JCTC Journal of Chemical Theory and Computation

pubs.acs.org/JCTC Article

Machine-Learned Kohn–Sham Hamiltonian Mapping for Nonadiabatic Molecular Dynamics

Published as part of Journal of Chemical Theory and Computation virtual special issue "First-Principles Simulations of Molecular Optoelectronic Materials: Elementary Excitations and Spatiotemporal Dynamics".

Mohammad Shakiba and Alexey V. Akimov*

Cite This: J. Chem. Theory Comput. 2024, 20, 2992–3007 Read Online

ACCESS | Metrics & More | Article Recommendations | Supporting Information

ABSTRACT: In this work, we report a simple, efficient, and scalable machine-learning (ML) approach for mapping non-self-consistent Kohn–Sham Hamiltonians constructed with one kind of density functional to the nearly self-consistent Hamiltonians constructed with another kind of density functional. This approach is designed as a fast surrogate Hamiltonian calculator for use in long nonadiabatic dynamics simulations of large atomistic systems. In this approach, the input and output features are Hamiltonian matrices computed from different levels of theory. We demonstrate that the developed ML-based Hamiltonian mapping method (1) speeds up the calculations by several orders of magnitude, (2) is conceptually simpler than alternative ML approaches, (3) is applicable to different systems and sizes and can be used for mapping Hamiltonians constructed with arbitrary density functionals, (4) requires a modest training data, learns fast, and generates molecular orbitals and their energies with the accuracy nearly matching that of conventional calculations, and (5) when applied to nonadiabatic dynamics simulation of excitation energy relaxation in large systems yields the corresponding time scales within the margin of error of the conventional calculations. Using this approach, we explore the excitation energy relaxation in C_{60} fullerene and $Si_{75}H_{64}$ quantum dot structures and derive qualitative and quantitative insights into dynamics in these systems.

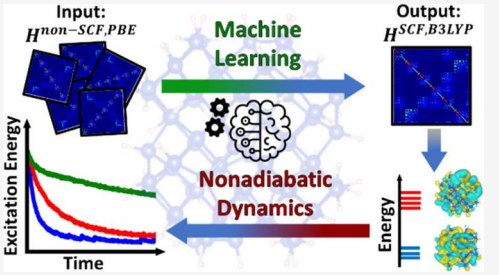

1. INTRODUCTION

The rise of solar energy harvesting materials such as semiconductor quantum dots (QD),[1,2] metal-halide perovskites,[3−7] or carbon nanotubes[8,9] offers sustainable and environmentally friendly alternatives to conventional energy production sources, such as fossil fuels or nuclear energy. However, the efficiency of photovoltaic materials is highly affected by the nonradiative energy loss processes, deteriorating the currently achievable efficiencies to ∼19% in the optimized multicomponent solar energy materials,[10,11] still far below the theoretical Schockley–Queisser limit.[12] Obtaining mechanistic insights into the underlying quantum processes in materials can help optimize their properties and efficiency. Nonadiabatic molecular dynamics (NA-MD) has proven itself as a powerful tool for modeling the evolution of excited states in various molecular and nanoscale systems and provided insights into charge transfer kinetics and mechanisms,[13−16] electron–hole recombination[17−21] and hot-carrier relaxation dynamics,[22−25] carbon dioxide reduction on metal oxide surfaces,[26,27] and water splitting.[28,29]

Simulation of excited state dynamics in nanoscale systems using NA-MD is a challenging problem and usually comes at a hefty computational price even when relying on various approximations.[30,31] The computational complexity of most NA-MD methods stems from the expense of the underlying electronic structure calculations. Density functional theory (DFT) is a widely used method for conducting the electronic structure calculations of large-scale molecular and periodic systems within NA-MD simulations. However, the relatively inexpensive pure density functionals, such as Perdew–Burke–Ernzerhof (PBE),[32] often used in this context can result in a significant underestimation of excited state energies, unphysical delocalization of excited state charge densities, especially within time-dependent-DFT (TD-DFT) calculations, and as a consequence can lead to a notable overestimation of excited state relaxation rates.[23,24,33] Adopting hybrid functionals can alleviate such problems but at a significantly increased cost of such calculations, making this strategy extremely demanding for modeling excited state dynamics in extended and nanoscale systems.

Received: January 4, 2024
Revised: March 17, 2024
Accepted: March 27, 2024
Published: April 6, 2024

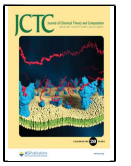

https://doi.org/10.1021/acs.jctc.4c00008
J. Chem. Theory Comput. 2024, 20, 2992–3007

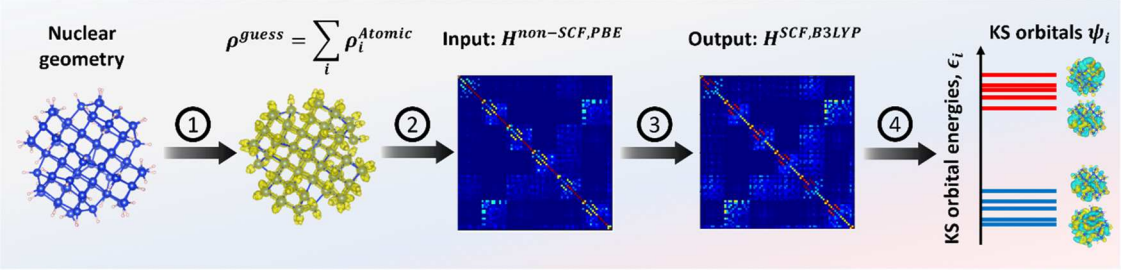

Figure 1. Illustration of the mapping Kohn−Sham Hamiltonian approach: (1) the initial geometry of the system of interest is used to compute a guess charge density, ρ_{guess}, given via the superposition of the atomic densities, ρ_i^{atomic}; (2) the guess charge density is used to construct a KS Hamiltonian matrix with the PBE density functional; (3) the ML is trained to map the non-self-consistent guess KS Hamiltonian with the PBE functional, $H^{non\text{-}SCF,PBE}$, to the self-consistent KS Hamiltonian with an arbitrary functional, such as the B3LYP functional in this example, $H^{SCF,B3LYP}$; (4) once the ML model is trained, the predicted KS Hamiltonian is constructed in one shot and is diagonalized to produce the desired properties such as molecular orbitals (MOs), ψ_i, and their energies, ϵ_i, which can be used in NA-MD calculations. The workflow is demonstrated by considering a $Si_{75}H_{64}$ QD as an example.

Recently, machine-learning (ML) techniques have gained a lot of popularity in different fields of computational chemistry as a way to speed up various types of calculations and surmount the problems that are too hard to treat with conventional methods. The ML approaches have helped accelerate rational drug and material discovery,[34,35] model photochemical or photocatalytic reactions,[36] predict reaction pathways, and investigate reaction mechanisms,[37−43] to name a few. There is a notable effort in using ML models to speed up molecular calculations, from using ML in the ML-based interatomic potentials[44−50] to their applications in the realm of electronic structure calculations.[51] In these applications, ML models are often designed to predict specific properties of a system such as its potential energy,[44−50] band gap,[52,53] molecular spectra,[54−57] and so on using the information about the system's geometry. The ML-based methods help substitute expensive quantum-chemical calculations by the computationally cheaper ML-based "surrogate" models that predict fundamental properties of molecular systems, such as their machine-learned interatomic potentials[51,58,59] or one-electron reduced density matrices.[60] This core information can then be used to compute the derived properties by standard formulas or methods.

Many works reported using ML in the context of quantum and nonadiabatic dynamics of excited states. For instance, Wang and co-workers[61] utilized ML to construct the Hamiltonian matrix elements for subsystems in graphene nanoribbons (GNR) on the basis of maximally localized Wannier functions. Combining this approach with the divide-and-conquer strategy, they have been able to conduct the direct NA-MD simulation of charge transport in GNRs with more than 10,000 atoms, although for up to a modest 10 fs in time. Rodríguez and Kananenka demonstrated the use of convolutional neural networks (CNN) to correctly predict the long-time dynamics in dissipative spin-boson systems.[62,63] Ullah and Dral used kernel ridge regression (KRR) to address a similar kind of problem.[55,64−66] Akimov utilized a multilayer perceptron with the periodically transformed time inputs (modes) to forecast the time series of TD-DFT-derived energy gaps and nonadiabatic couplings of monolayer black phosphorus to extend the time scales accessible to NA-MD simulations to dozens of picoseconds.[67] Prezhdo and co-workers utilized ML-based force fields to enable several-hundred-picoseconds-long simulations of classical dynamics of perovskites.[68] Such simulations have helped sample rare effects of appearance of deep trap states, which lead to a notable difference of the computed recombination time scales as compared to idealized small-supercell models. They also utilized ML approaches to analyze the NA-MD simulations to learn effective reaction coordinates for nonradiative relaxation/carrier recombination in such systems.[69] In another work, the Prezhdo group utilized the ML-based force field to sample long MD trajectories of perovskite systems. Such trajectories were used to construct the vibronic Hamiltonians by using the inverse fast Fourier transform approach.[70] Cignoni et al.[71] developed an ML model to predict the full exciton Hamiltonian in photosynthetic complexes using a Gaussian process regressor. Using a rotationally invariant ML approach, Chandrasekaran et al.[72] showed how one can bypass solving the Kohn−Sham (KS) equations by directly predicting the electronic structure of materials. Tretiak and co-workers used NNs to model exciton-polaritons in azomethane[73] and plasmon dynamics in Ag nanoparticles.[74] Westermayr et al.[75] combined SchNet model[76,77] with SHARC[78] to perform trajectory surface hopping[79,80] for excited states dynamics in $CH_2NH_2^+$, CSH_2, and SO_2 molecules. Others adopted deep NNs and KRR method to predict potential energy surfaces of polyatomic molecules for NA-MD simulations.[81,82] In separate works of Yaron,[83] Tretiak,[84] and Miller groups,[85] an ML approach was utilized to improve the accuracy of various semiempirical methods for bioorganic and organic materials.

In both modes, whether it is to directly predict the properties needed for quantum dynamics calculations (such as energies and couplings) or to predict the surrogate Hamiltonian matrix elements or density matrices, the ML models must be constructed using appropriate inputs (coordinates or, more generally, descriptors) and training data. Often, the ML methods rely on the direct usage of global descriptors such as traditional real-space atomic coordinates of the systems,[86−89] including internal coordinates[90−92] or normal modes.[58,93] Although such approaches are well defined and can be quite convenient in certain situations, this strategy is limited by the need to use a large amount of data for the training, which can range from tens of thousands to millions of data points. For example, the SchNOrb model[94] is one of the most famous ML models for predicting the Hamiltonian matrix, but it requires optimizing nearly 93 million parameters to be able to compute the Hamiltonian matrix with just a little more than 100 basis functions. The training time takes more than 80 h on graphics processing unit (GPU)-accelerated

https://doi.org/10.1021/acs.jctc.4c00008
J. Chem. Theory Comput. 2024, 20, 2992−3007

supercomputers for small systems such as ethanol or uracil, which makes the preparation of the testing and training data set cumbersome and at least as time-consuming as doing the direct dynamics.

Other strategies employ descriptors such as time,[67] Coulomb matrices,[95] inverse internuclear distances,[96,97] smooth overlaps of atomic positions,[98] and more.[82,99−101] Unfortunately, using the time variable as the sole independent input variable to ML model as in ref 67 is based on the idea of implicit trajectories, where the ML-predicted time-dependent properties (scalar nonadiabatic coupling (NACs) or state energies) may be computed without having any information on the system's geometry, which may make the analysis of the obtained results incomplete. Having an ML model that is explicitly geometry-dependent, enables predicting fundamental properties of the system (e.g., orbitals and Hamiltonians), does not require heuristic guess of the best training coordinates, and is not too expensive to construct and train is the desirable goal.

In this work, we approach the ML-based surrogate Hamiltonian construction from a different angle: instead of relying on atomic coordinates as the direct inputs to train the ML model, we effectively use the coordinate-dependent atomic-guess Kohn−Sham (KS) Hamiltonian matrix as an input. This input is used to predict the converged KS Hamiltonian at a desired level of theory, which can be used to compute the resulting KS orbitals and other derived properties (energies and time-overlaps) needed for NA-MD calculations (Figure 1). In this approach, we leverage our observation that the KS Hamiltonian with the converged charge density is often a close and rather smooth map of the initial guess KS Hamiltonian. The latter is a geometry-sensitive property and is fast to compute, even for large complex systems. One can further establish a mapping of such a guess KS Hamiltonian computed at a lower level of theory, e.g., with a pure density functional, such as PBE, or even tight-binding (TB) models such as the extended tight-binding (xTB),[102,103] to the converged KS Hamiltonians constructed at a higher level of theory, such as hybrid functionals, perturbation theory, or configuration interaction methods. One can regard this approach as a form of preprocessing of the atomic geometry information before it is used in construction of the ML model. As opposed to using the atomic geometries directly, this preprocessing makes it possible to significantly reduce the number of data points that should be used in the training set, leading to a more robust and efficient ML methodology for NA-MD calculations. As a demonstration, we show how this method can be applied to study excited state relaxation dynamics in C_{60} and $Si_{75}H_{64}$ QD.

The ML-based NA-MD approach presented in this work is formulated for systems whose nuclear dynamics is not strongly perturbed by electronic excitations, the so-called neglect of the back-reaction approximation (NBRA, vide infra). The standard NBRA NA-MD computations typically involve precomputed nuclear trajectories (guiding trajectories)[104] that parametrize the electronic dynamics of a system. While the guiding trajectories may be obtained relatively inexpensively using adiabatic molecular dynamics with force fields,[105−107] semi-empirical[108] or xTB methods,[21,109,110] the propagation of electronic dynamics requires more expensive DFT calculations. Obtaining accurate energies and time overlaps may require the use of expensive hybrid functionals, with the steeply increased computational expenses.[33] This task may be out of reach for large systems, especially if such calculations are to be done for hundreds and thousands of time steps along the guiding trajectory. This is where the ML-based KS Hamiltonian mapping approach presented in this work would come in handy.

The computational acceleration offered by the present method comes in three flavors: (1) due to substituting the self-consistent calculations with the non-self-consistent ones (about an order of magnitude acceleration); (2) due to replacing expensive hybrid functional calculations by those relying on pure functionals (an arbitrary order of magnitude increases rapidly with the size of the system and the basis set size); and (3) due to utilizing only a fraction of geometries of the guiding trajectory at the ML training step (an acceleration by an order of magnitude or more increases with the length of the target NA-MD simulations to conduct). As an illustration, one can think of a hypothetical task of conducting a 10 ps NA-MD (that is 10,000 geometries, an upper edge of what is used in typical direct NBRA NA-MD) calculation for a C_{60} system with the electronic states described at the B3LYP level. With the current approach, one may end up needing to do only 100 SCF calculations at the B3LYP level and 100 non-SCF calculations at the PBE level to construct the ML model that would map the non-SCF PBE KS Hamiltonian, $H^{\text{non-SCF,PBE}}$ to the SCF B3LYP one, $H^{\text{SCF,B3LYP}}$ for arbitrary nuclear geometries. The "production" calculations would include 10,000 non-SCF calculations at the PBE level (relatively cheap) to obtain the B3LYP-level electronic structure. This hypothetical process would result in a 100-fold acceleration of the NBRA NA-MD workflow. Of course, one can envision the mappings of even cheaper non-SCF Hamiltonians such as DFTB or xTB to SCF KS Hamiltonians or mappings to even more computationally expensive many-electron Hamiltonians such as those of TD-DFT, CAS, GW, and so on. Such mappings would deliver even higher accelerations of the NBRA-based NA-MD calculations, but this kind of mapping is outside of the scope of the present work.

Having identified the sources of possible acceleration of the ML-based KS Hamiltonian mapping approach, we do not take full advantage of such acceleration in this work, as we aim to not only demonstrate the acceleration but also assess the reliability of the methodology. For this reason, the NA-MD calculations with the ML-based mapped Hamiltonians are also conducted using the directly computed self-consistent DFT Hamiltonians, including those with the hybrid functionals. Although such calculations are rather expensive, they provide a direct assessment of the applicability of the ML-mapped KS Hamiltonians to the NA-MD simulations as well as estimates of the training set sizes needed to achieve reasonable performance of the method. Although such an estimate is not guaranteed to be transferable to other systems, it may be a useful guiding number for future applied studies, where the computational acceleration offered by the method could be fully leveraged.

2. THEORY AND METHODS

2.1. Nonadiabatic Molecular Dynamics Methodology.

Here, we briefly overview the theory of nonadiabatic molecular dynamics (NA-MD) used in the present work. A more detailed account can be found elsewhere.[30] The evolution of the electronic wave function is described by the time-dependent Schrodinger equation (TD-SE):

https://doi.org/10.1021/acs.jctc.4c00008
J. Chem. Theory Comput. 2024, 20, 2992−3007

$$i\hbar\frac{\partial\Psi(r, R(t))}{\partial t} = \hat{H}_{el}(r, R(t))\Psi(r; R(t)) \quad (1)$$

where r and $R(t)$ represent the electronic and nuclear coordinates, respectively. In the quantum-classical trajectory-surface hopping (TSH) methods, the effective Hamiltonian operator appearing in eq 1 is essentially the electronic Hamiltonian operator, $\hat{H}_{el}$, since the nuclei are treated classically and the corresponding nuclear kinetic energy operator disappears. The nuclear trajectory is obtained using classical adiabatic MD (although with the forces that may be derived from quantum chemical calculations) and is then used as the guiding trajectory to compute the electronic Hamiltonians. In this work, we utilize the NBRA approximation of Prezhdo et al.[111−113] according to which the electronic excitation is assumed not to affect the nuclear dynamics significantly, and which has been demonstrated to yield reasonable results for many nanoscale[13,21,23,24,114−118] and rigid molecular systems.[108,119,120] Accordingly, only the adiabatic ground state forces are needed to precompute nuclear trajectories, even if electronic transitions occur. In the NBRA approach, electronic transitions do not lead to nuclear trajectory branching and, vice versa, are determined by the precomputed nuclear trajectory.

The adoption of the NBRA is based on the assumption that no bond breaking or major structural reorganization occurs during the dynamics, which has been demonstrated to be reasonable for relatively "rigid" systems such as fullerenes or nanoparticles,[13,23,115,121,122] as well as for periodic and condensed-matter systems.[17,21,22,24,28,123,124] As a result, nuclear geometries sampled along the guiding trajectory are relatively close to each other in a configurational space. Consequently, the ML model based on the linear regression kernel is likely to yield reasonable results for snapshots of the guiding trajectory that have not been seen during the training. In this regard, presenting independent guiding trajectories to the training pool for constructing the ML model may not lead to significant changes in ML quality. In fact, even standard NBRA NA-MD calculations often utilize a single but sufficiently long guiding trajectory.[23,109,123,124]

Developing the ML approach for non-NBRA simulations may be more difficult since multiple divergent trajectories could be produced due to stronger branching of the dynamics, necessitating larger sampling sizes and potentially requiring more complex kernels for ML models. Furthermore, if one desires to utilize the ML mapping approach to guide the nuclear trajectories, then the forces would need to be computed. Since the present approach maps the non-SCF Hamiltonians to the SCF ones only to a certain precision, which is still below the typical thresholds needed for accurate force calculations, in the present approach we do not aim to compute forces to generate new guiding trajectories. Such a possibility should still be achievable but remains outside the scope of this work.

The total wave function, Ψ, is written as a linear combination of M dynamical basis functions, $\{\psi_i, i = 0,\cdots M-1\}$:

$$\Psi(r; R(t)) = \sum_{i=0}^{M-1} C_i(t)\psi_i(r; R(t)) \quad (2)$$

In the above notation, the semicolon in parentheses represents the parametrical dependence of the Hamiltonian operator and dynamical basis function on nuclear coordinates, sampled along the guiding trajectory, $R(t)$.

In the basis of dynamical basis functions, eq 1 can be rewritten to yield the equation describing the evolution of the $C_i(t)$ coefficients as

$$i\hbar\dot{C}_i(t) = \sum_j H_{ij}^{vib}(t)C_j(t) \quad (3)$$

where $H_{ij}^{vib}(t) = E_j(R(t))\delta_{ij} - i\hbar d_{ij}(R(t))$ are the elements of the vibronic Hamiltonian matrix, $E_j(R(t))$ is the energy of the jth dynamical basis function and $d_{ij}(R(t))$ is the time-derivative nonadiabatic coupling (NAC) between jth and ith states at nuclear geometry of $R(t)$:

$$d_{ij} = \langle\psi_i(r; R(t))\left|\frac{\partial}{\partial t}\right|\psi_j(r; R(t))\rangle \quad (4)$$

In the present work, the dynamical basis functions, $\{\psi_i\}$ are chosen as the excited Slater determinants, Φ_a^b, constructed from a subset of the KS orbitals, $\{\phi_a^{KS}\}$ of the chosen KS Hamiltonian, $\hat{H}^{KS}$:

$$\psi_i = \Phi_a^b = \hat{a}_b^+\hat{a}_a\Phi_0 \quad (5)$$

Here, $\hat{a}_b^+$ and $\hat{a}_a$ are the Fermionic creation and annihilation operators, respectively, and Φ_0 is the ground state determinant so that the determinant Φ_a^b corresponds to electronic excitation between KS orbitals a and b of the same spin: $\phi_a^{KS} \rightarrow \phi_b^{KS}$. The KS orbitals $\{\phi_a^{KS}\}$ are the eigenfunctions of the KS Hamiltonian, $\hat{H}^{KS}$:

$$\hat{H}^{KS}(r; R(t))\phi_a^{KS}(r; R(t)) = \epsilon_a(R(t))\phi_a^{KS}(r; R(t))) \quad (6)$$

The energies of the dynamical basis functions, E_i, are computed from the KS orbital energies, ϵ_a, as

$$E_i = \epsilon_b - \epsilon_a \quad (7)$$

To account for possible state crossings and phase inconsistencies of the dynamical basis functions along the guiding trajectories, eq 3 is integrated using the local diabatization approach:[125]

$$C(t + \Delta t) = T\exp\left(-\frac{E(t) + T^+E(t + \Delta t)T}{2\hbar}\Delta t\right)C(t) \quad (8)$$

Here, E is the diagonal matrix of energies of the dynamical basis functions, $C = (C_0, C_1, \cdots C_{M-1})^T$ is the vector of the dynamical basis amplitudes, $\hbar$ is the reduced Planck's constant ($\hbar = 1$ in atomic units adopted internally), and T is the orthogonalized basis reprojection matrix, computed as

$$T = X(P^{-1}) \quad (9a)$$

$$X(A) = A(A^+A)^{-1/2} \quad (9b)$$

$$P: P_{ij} = \langle\psi_i(t)|\psi_j(t + \Delta t)\rangle \quad (9c)$$

Here, P is the time-overlap matrix. It is used not only to evolve the TD-SE by the local diabatization approach shown above, but also to numerically compute the scalar NACs, eq 4, using the Hammes−Schiffer−Tully formula,[126] $d_{ij}\left(t + \frac{\Delta t}{2}\right) \approx \frac{P - P^+}{2\Delta t}$. In our computations, the wave functions $\{\psi_i\}$ are given by excited Slater determinants. The time-overlaps between such

https://doi.org/10.1021/acs.jctc.4c00008
J. Chem. Theory Comput. 2024, 20, 2992−3007

functions are computed using the Lowdin formula[127] as detailed elsewhere.[109]

The coefficients $C(t)$ are used to compute the probabilities of the stochastic hops between states. We use the simplest and one of the most popular TSH schemes—the fewest switches surface hopping (FSSH) of Tully.[80] According to the FSSH, the hops between states i and j are proposed with the probability of:

$$P_{i\to j}^{\text{prop}}(t,\, t+\Delta t) = \frac{\Delta t}{\rho_{ii}}\text{Im}\left(\rho_{ij}\left(t+\frac{\Delta t}{2}\right)H_{ji}^{\text{vib}}\left(t+\frac{\Delta t}{2}\right) - H_{ii}^{\text{vib}}\left(t+\frac{\Delta t}{2}\right)\rho_{ji}\left(t+\frac{\Delta t}{2}\right)\right) \tag{10}$$

where $\rho_{ij}(t) = c_i(t)c_j^*(t)$ are the elements of the reduced density matrix. The hop $i \to j$ is considered proposed (attempted) if $\xi < P_{i\to j}^{\text{prop}}$, where ξ is a random number uniformly distributed on the $[0, 1]$ interval. The proposed hops may or may not be accepted to reflect the detailed balance between electronic and nuclear energy partitioning.

In the original FSSH prescription of Tully, hop acceptance is decided based on the possibility to rescale nuclear velocities along the derivative coupling vector of a given pair of states. However, within the NBRA approach, this criterion is simplified by using the Boltzmann factor:[104]

$$P_{i\to j}^{\text{acc}}\left(t+\frac{\Delta t}{2}\right) = \min\left(1,\, \exp\left(-\frac{E_j - E_i}{K_B T}\right)\right) \tag{11}$$

The proposed hop $i \to j$ is considered accepted if $\zeta < P_{i\to j}^{\text{acc}}$, where ζ is a random number uniformly distributed on the $[0, 1]$ interval. Otherwise, the hop is considered frustrated.

The coefficients $C(t)$ coherently evolved according to eq 9a–9c can be altered to account for decoherence effects. Here, we consider two simple decoherence correction schemes—the instantaneous decoherence at the attempted hops (ID-A)[128] and the modified simplified decay of mixing (mSDM).[129,130]

In the ID-A approach, in addition to the FSSH prescription of state hops and the underlying coherent evolution, the amplitude vector C is collapsed at every proposed hop:

$$C \to \tilde{C} = (0,\, 0,\, \cdots \exp(i\arg(C_i)),\, \cdots,\, 0,\, \cdots) \tag{12}$$

The index i selects the state onto which the coherent superposition is collapsed: if the hop is not successful (frustrated), the index i is chosen as the current active state. If the hop is successful, then the coefficient i is chosen as the new state onto which the hop has occurred.

In the second decoherence correction scheme, the mSDM, the coherent amplitudes, C, are modified gradually at every time step, before they are used to compute hopping probabilities in eq 10:

$$C_i \to \tilde{C}_i = C_i \exp\left(-\frac{\Delta t}{\tau_{if}}\right),\ \forall\ i \neq f \tag{13a}$$

$$C_f \to \tilde{C}_f = C_f\sqrt{\frac{1 - \sum_{i\neq f}|\tilde{C}_i|^2}{|C_f|^2}} \tag{13b}$$

Here, f is the index of the currently active state and τ_{ij} is taken to be the pure dephasing rate between states i and j. According to the mSDM prescription,[129] these are computed according to the formula of Akimov and Prezhdo:[131]

$$\tau_{ij}^{-1} = \sqrt{\frac{5\langle \delta E_{ij}^2\rangle}{12\hbar^2}} \tag{14}$$

where $\langle \delta E_{ij}^2\rangle$ is the trajectory (ideally, and ensemble) average of the energy gap fluctuation, $\delta E_{ij} = E_i - E_j - \langle E_i - E_j\rangle$.

Counting the number of stochastic trajectories in every electronic state at a given time, $N_i(t)$, we compute TSH-based populations as

$$P_i^{\text{SH}}(t) = \frac{N_i(t)}{N} \tag{15}$$

where $N = \sum_{i=0}^{M-1} N_i$ is the total number of stochastic trajectories. The state populations, P_i^{SH}, are used to compute time-dependent excitation energy excess as

$$E(t) = \sum_{i=1}^{M-1} P_i^{\text{SH}}(t)[E_i(t) - E_1(t)] \tag{16}$$

where E_i is the energy of the excited state i. The relaxation time scales are computed by fitting the excess energy decay with a stretched−compressed exponential function of the form:

$$E(t;\, E_0,\, \tau,\, \beta) = E_0 \exp\left(-\left(\frac{t}{\tau}\right)^{\beta}\right) \tag{17}$$

where E_0 corresponds to the initial excitation energy excess level. Fits with $R^2 > 0.5$ are selected for computing the average and error bars. The use of stretched−compressed exponential fitting function may be tracked back to the work of Williams and Watts[132] who noted that dielectric dispersions and absorptions in many systems do not follow a single relaxation time scale. Such a fitting function has also been used in works on modeling of excitation energy relaxation dynamics in complex systems with dense manifolds of excited states.[121,133]

2.2. Computational Details: Electronic Structure Calculations. For electronic structure calculations, both C_{60} and $Si_{75}H_{64}$ QD structures are first centered in the simulation box, and a vacuum of 7 Å is added to each side of the box. The MD calculations sample 3000 steps from the canonical ensemble via velocity rescaling thermostat[134] with a target temperature of 300 K. In the MD calculations, the forces are obtained using the PBE functional[32] together with the Grimme's DFT-D3 dispersion correction.[135] The timesteps for C_{60} and $Si_{75}H_{64}$ structures are 1.0 and 0.5 fs, respectively. The smaller time step is used for the $Si_{75}H_{64}$ QD system because it contains light hydrogen atoms. Out of the total 3000 MD snapshots, the last 2000 geometries are selected to compute the properties needed for NA-MD calculations and used in training ML models.

In this work, three density functions are used for computing time overlaps, eq 9c, and state energies: PBE,[32] three-parameter Becke−Lee−Yang−Parr (B3LYP),[136−139] and Heyd−Scuseria−Ernzerhof (HSE06).[140,141] In all electronic structure calculations, valence electrons are described using the SZV-MOLOPT-GTH[142−144] basis set, while the effect of core electrons, if accounted for, with Goedecker−Teter−Hutter pseudopotentials.[142] Self-consistent field (SCF) calculations are done with a charge density convergence limit of 5.0×10^{-7} Bohr^{-1} and a charge density cutoff of 300 Ry. In this work, we adopt nonperiodic calculations for both structures which correspond to a single K-point at (0, 0, 0), the Γ point. The electronic structure calculations are conducted using the CP2K[145,146] software package. The KS Hamiltonian matrices

https://doi.org/10.1021/acs.jctc.4c00008
J. Chem. Theory Comput. 2024, 20, 2992−3007

and the molecular orbitals coefficients are printed by CP2K in the atomic orbital basis for each geometry and then parsed by Libra code[105,106] into Python. The same procedure is done for all geometries to generate the atomic-guess Hamiltonian matrices using PBE but with only 1 SCF step. The atomic-guess Hamiltonian is the Hamiltonian that is evaluated at the electron density given by the superposition of atomic densities. This Hamiltonian is computed as a one-shot, non-self-consistent Hamiltonian.

2.3. Computational Details: NA-MD Simulations. For NA-MD calculations, we first build a mixed electron and hole excitation basis by exciting electrons from the occupied to the unoccupied orbitals near the band edge. For C_{60}, the excited state basis is built from all single excitations from the first 14 occupied orbitals near the valence band edge to the first 6 unoccupied orbitals from the conduction band edge (Figures S1 and S2). For the $Si_{75}H_{64}$ QD, the excited state basis includes all excitations from the first 10 occupied orbitals to the first 10 unoccupied orbitals (Figures S1 and S2). Ideally, one would want to go beyond the single-particle (formulated either through the bare KS orbitals or through Slater determinants) picture into something like configuration interaction singles (CIS) or TDDFT. In fact, such a capability is already present in the Libra code and has been used in a previous study.[23] At the same time, the use of the single-particle picture is also a common practice in modeling excited state dynamics in large systems[22,28,115,121] the choice dictated by computational costs of the many-determinantal methods. In addition, lower excited states are often dominated by a single determinant.[23] Since the present work aims to assess the quality of the ML-mapped KS Hamiltonians for NA-MD purposes, we choose a single-particle description of electronic states, expecting that the obtained relaxation time scales may not be the definitive characterization of the quantum dynamics of true excited states.

The initial electronic state is chosen as follows: for the C_{60} fullerene, any state among the five excited states in the S_2 band (Figure S2a−c), for the $Si_{75}H_{64}$ QD, any state among three excited states with energy of ∼0.7 eV above the first excited state are initially populated (Figure S2d−f).[23] As Figure S2 demonstrates, the electronic states in C_{60} form bands of quasi-degenerate states, S_1 and S_2, separated by a notable gap. For Si QD there are no clearly defined bands, as all states are rather close to each other in energy. Due to the closeness of the individual states belonging to the same band, the initial states are chosen by randomly selecting individual states within the band of interest. Such a selection aims to be done within a certain excitation energy window, corresponding to experimental setups when possible.

The NA-MD simulations start from 10 initial geometries in the MD trajectory. 250 stochastic realizations of the TSH method are utilized. The electronic integration time step for NA-MD is selected as 1.0 and 0.5 fs for C_{60} and $Si_{75}H_{64}$ QD structures, respectively. Considering that we have only 2000 MD steps in each guiding trajectory, sampling 10 initial geometry every 200 steps would not allow long NA-MD simulations. To produce the 1 ps NA-MD trajectories, we use the Hamiltonian repetition approach that consists of looping over the initial 1 ps data set of Hamiltonians obtained along the guiding trajectory. This technique has been widely used in the NBRA-based NA-MD calculations[18,21,109,116,123,124,147] although it is known to under- or overestimate the resulting time scales by nearly an order of magnitude.[148] However, since the same approach is applied equally to both the ML and direct simulations, it should not affect the validity of the current study, although the absolute values of the excitation decay time scales may not be quantitative compared to experiment. NA-MD calculations are done using Libra code,[105,106] version 5.5.0. All input files and Python codes pertinent to this study are freely available via Zenodo repository.[149]

2.4. Machine Learning. In this section we outline the main procedure of our current approach, establishing a mapping of the atomic-guess KS Hamiltonian (inputs to the ML model) to the KS Hamiltonian that corresponds to a converged charge density (outputs of the ML model). In particular, we use the atomic-guess Hamiltonians computed with the PBE[32] functional, while the converged Hamiltonians are obtained with the PBE,[32] B3LYP,[136−139] and HSE06[140,141] functionals. We employ the linear KRR approach, which is a least-squares optimization problem with the L_2 regularization, as implemented within the Scikit-learn package.[150] Both input and output matrices are symmetric $N_{AO} \times N_{AO}$ matrices, where N_{AO} is the number of atomic orbital functions. For large systems, such data may be more difficult to use directly in the ML training procedure, in terms of both the efficiency of the underlying computations and the capacity of the ML to correctly learn the multidimensional patterns. To increase the efficiency and reliability of the ML training, we leverage the symmetry of the Hamiltonians on the AO basis and use only the upper triangular part of the KS Hamiltonian matrix together with its diagonal elements for training. The upper triangular matrices are vectorized before they are used in the ML training. The corresponding input and output vectors are therefore of $\frac{N_{AO}(N_{AO}+1)}{2}$ size each. The vectorized matrices are further split into multiple data sets (segments) and are used to construct separate ML mapping functions/models (see Section S2 in the Supporting Information). The input and output data are preprocessed separately for each segment according to the standard scaling procedure of the scikit-learn package.[150] This procedure involves shifting and scaling of the data to bring it to zero mean and a standard deviation of 1.0.

At first glance, the splitting procedure may introduce some inconsistency, but the use of unsegmented data for the ML model training may be not practical for large systems where the vectorized matrices may have millions of elements (features). This approach also helps parallelize the calculations for large KS Hamiltonian matrices. There could be different splitting approaches for dividing the vectorized upper triangular of a KS Hamiltonian matrix (see Section S2 in the Supporting Information for a more detailed discussion). In this work, we adopt one of such possible strategies: split the vector into multiple subvectors of similar size (see Figure S3b in the Supporting Information).

In the present approach, we use the linear KRR model, which can be briefly exemplified as follows. To predict each segment of the vectorized upper triangular part of the self-consistent KS Hamiltonian matrix computed with say a B3LYP functional at a given trajectory point, $\boldsymbol{R}(t_\alpha)$, the corresponding segments of the vectorized upper triangular part of the non-self-consistent KS Hamiltonians computed with the PBE functional at other points are used:

https://doi.org/10.1021/acs.jctc.4c00008
J. Chem. Theory Comput. 2024, 20, 2992−3007

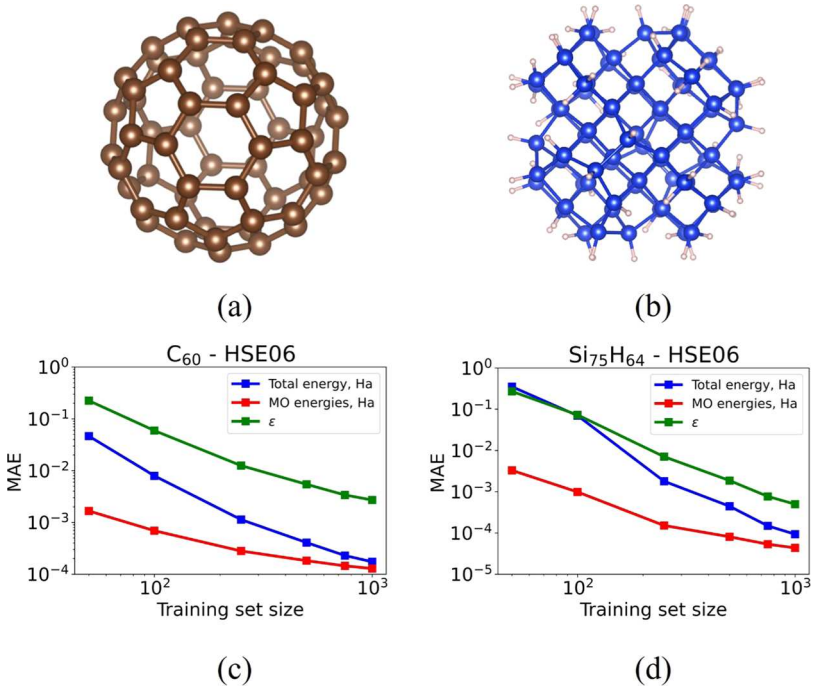

Figure 2. Molecular structures of (a) C_{60} fullerene and (b) the $Si_{75}H_{64}$ QD. MAE of total energy, MOs' energies, and ϵ, eq 19b, for (c) C_{60} and (d) $Si_{75}H_{64}$ QD using the HSE06 functional. The unit of each property is shown in the legend box.

$$\begin{aligned}&\mathrm{vec}[\boldsymbol{H}^{\mathrm{B3LYP,SCF}}(\boldsymbol{R}(t_\alpha))]\\&= \mathrm{vec}[\boldsymbol{H}^{\mathrm{B3LYP,SCF}}(\mathrm{vec}[\boldsymbol{H}^{\mathrm{PBE,non\text{-}SCF}}(\boldsymbol{R}(t_\alpha))])]\\&= \sum_{\beta=1}^{N_{\mathrm{train}}} \boldsymbol{K}(\mathrm{vec}[\boldsymbol{H}^{\mathrm{PBE,non\text{-}SCF}}(\boldsymbol{R}(t_\alpha))]\\&\quad, \mathrm{vec}[\boldsymbol{H}^{\mathrm{PBE,non\text{-}SCF}}(\boldsymbol{R}(t_\beta))])\boldsymbol{c}_\beta\end{aligned} \tag{18}$$

where N_{train} is the size of the training set and $\boldsymbol{K}(\mathrm{vec}[\boldsymbol{X}],\mathrm{vec}[\boldsymbol{Y}]) = \mathrm{vec}[\boldsymbol{X}](\mathrm{vec}[\boldsymbol{Y}])^T$ is the kernel function for vectorized forms of the input matrices $\mathbf{X}$ and $\mathbf{Y}$—$\mathrm{vec}[\boldsymbol{X}]$ and $\mathrm{vec}[\boldsymbol{Y}]$, respectively. The KRR coefficients $\boldsymbol{c}_\beta$ (vectors themselves) are computed as $\boldsymbol{c}_\beta = (\boldsymbol{K} + \lambda \boldsymbol{I})^{-1}\mathrm{vec}[\boldsymbol{H}^{\mathrm{B3LYP,SCF}}(\boldsymbol{R}(t_\beta))]$, where λ is a hyperparameter used to prevent overfitting.[151] The regularization parameter is chosen by trial and error and is fixed and selected as a value of 1.0. Here, both $\mathrm{vec}[\boldsymbol{H}^{\mathrm{PBE,non\text{-}SCF}}]$ and $\mathrm{vec}[\boldsymbol{H}^{\mathrm{B3LYP,SCF}}]$ are vectors that represent the same segments of the split-vectorized upper triangular part of the corresponding KS Hamiltonian matrices, $\boldsymbol{H}^{\mathrm{PBE,non\text{-}SCF}}$ and $\boldsymbol{H}^{\mathrm{B3LYP,SCF}}$. Unlike in training of nonlinear NNs, such as multilayer perceptron model, the parameters in the linear KRR model are computed analytically and can be regarded as the optimal for the kind of model chosen. To achieve even higher accuracy, one can adopt a higher degree of polynomial functions in KRR or use more complicated ML models such as convolutional or nonlinear kernels NNs. At the present stage, the developed ML approach does not guarantee rotational invariance/equivariance,[152] and is yet to be refined to address this conceptual shortcoming.

To train the ML model, we sampled 2000 geometries using the ab initio MD calculations. The results obtained for these 2000 time steps are regarded as the reference and are used to assess the reliability of the current approach. As alluded to in the Section 1, our goal here is to demonstrate that one can use a small subset of the snapshots from the guiding trajectory points together with the corresponding electronic structure data and produce an ML model that would be able to inexpensively predict the electronic structure data for the other trajectory snapshots. One of the questions we ask is what the minimal size of the data needed is to train a sufficiently accurate ML model that could be used in the NBRA NA-MD simulations. Thus, we consider training sets of different sizes, ranging from 50 (2.5%) to 1000 (50%) geometries from the MD trajectory. The rest of the trajectory time steps are used to evaluate the performance of the trained ML model (the test set). The quality of the ML model is evaluated by computing: (a) the mean absolute error (MAE) of the total energy; (b) the MAE of MO energies; (c) the MAE of the quantity ϵ, eq 19a and 19b, that characterizes shapes of the predicted KS orbital:

$$\epsilon_{i,\mathrm{overlap}} = 1.0 - |\langle \psi_{i,\mathrm{ML}} | \psi_{i,\mathrm{ref}} \rangle| \tag{19a}$$

$$\epsilon = \frac{1}{N_{\mathrm{MO}}} \sum_{i=1}^{N_{\mathrm{MO}}} \epsilon_{i,\mathrm{overlap}} \tag{19b}$$

where $\psi_{i,\mathrm{ref}}$ is the reference ith MO from the self-consistent calculations, $\psi_{i,\mathrm{ML}}$ is the MO obtained by diagonalizing the ML-predicted Hamiltonian, and N_{MO} is the number of MOs. The MAE is computed by using only the test data points.

3. RESULTS AND DISCUSSION

We demonstrate the capability of the developed method by applying it to the model NA-MD in two extended molecular systems: C_{60} fullerene and $Si_{75}H_{64}$ QD (Figure 2a,b).

Having an accurate mapping of the guess PBE input to the converged B3LYP or HSE06 output is of paramount significance since the converged (self-consistent) electronic structure calculations with the hybrid functionals can be orders of magnitude more expensive than constructing the non-self-consistent (based on the atomic density superposition) Hamiltonians with pure density functionals such as PBE. Within the context of NA-MD calculations, the electronic

https://doi.org/10.1021/acs.jctc.4c00008
J. Chem. Theory Comput. 2024, 20, 2992−3007

structure calculations must be performed for multiple MD timesteps. In order to gain a notable acceleration, one must be able to use a minimal amount of self-consistent electronic structure calculations with the target functional as the training data points. At this expense, a reliable ML model is constructed and enables one to quickly construct the surrogate KS Hamiltonian at the target level of theory for the rest of the nuclear geometries.

The ML models are trained until the training set reaches $\sim 10^{-5}$ and $\sim 10^{-6}$ Ha MAE of the Hamiltonian matrix elements for C_{60} and $Si_{75}H_{64}$ QD, respectively (Section S3 in the Supporting Information, Figure S4). These values are achieved for all of the target functionals considered. Using only 250 geometries (12.5% of the available data) in the training set, the MAE for the testing already reaches values below 10^{-4} and 10^{-5} Ha in the Hamiltonian matrix elements error for C_{60} and $Si_{75}H_{64}$ QD, respectively, and less than 10^{-3} Ha in total energy for both structures, which is less than the chemical accuracy (1 kcal/mol). The only case in which the ML model shows a higher total energy error is for $Si_{75}H_{64}$ QD using the B3LYP functional with an MAE of ~2.74 kcal/mol. The testing error reaches the training error as the size of the training set increases such that the training and the testing sets coincide. By using 250 geometries in the training set, the MAE of all MOs' energies reaches about 10 meV for C_{60} and 3 meV for $Si_{75}H_{64}$ QD (Figures 2 and S3, S4). The average deviation of the overlaps of all predicted MOs with the converged results from 1.0, ϵ, is less than 10^{-2} for both structures showing that the MOs obtained via ML pathway are very close to the reference orbitals obtained with the self-consistent KS Hamiltonian (Figures 2 and S4, S5). These are rather impressive characteristics of the ML's ability to reproduce the electronic structure data for complex systems considering the modest sizes of the training sets used and the simplicity of the ML model. Extending the size of the training sets is a straight, although a rather brute-force route to improving these characteristics (Figure 2). Using more sophisticated ML kernels, preprocessing the data, and improving the sampling criteria for the training set selections may be next-level strategies, but such investigation goes beyond the present proof-of-the-principle work.

Considering the ML approach yields a reasonable accuracy predicting the total and orbital energies as well as in KS orbitals themselves, we further assess the computational efficiency of this method in contrast to conventional electronic structure calculations, as detailed in Section S4 in the Supporting Information. Already for the modestly sized C_{60} and $Si_{75}H_{64}$ QD systems, we observe an order of magnitude acceleration when using pure density functional and 2−3 orders of magnitude acceleration when using hybrid functionals (Table 1). The speed-up factor is greater for hybrid functionals since such calculations are computationally demanding if conducted in a conventional way, with their time scaling as $O(N_{bas}^4)$, where N_{bas} is the number of the basis functions. In contrast, the ML approach requires only quadratically scaling time, $O(N_{bas}^2)$, to construct the KS Hamiltonian. In principle, since our approach also requires the KS Hamiltonian diagonalization, for larger systems, one would require a cubic time, $O(N_{bas}^3)$, unless lower-scaling techniques are employed. The smaller speed-up factors obtained for the PBE functional can be attributed to weaker scaling of the original PBE calculations, $O(N_{bas}^3)$, compared with that of the hybrid functionals. For the PBE calculations, we also observe a counterintuitive larger acceleration for the smaller C_{60} compared to the $Si_{75}H_{64}$ QD. This can be explained by the more tight-binding nature of $Si_{75}H_{64}$ QD MOs compared to the more delocalized MOs of C_{60}. As a result, the conventional PBE calculations of the $Si_{75}H_{64}$ QD require fewer SCF iterations to get converged orbitals than those of C_{60} (Table S1). Finally, when the speed-up factors are thought of in absolute numbers, the comparison strongly favors the ML approach. For instance, the SCF calculations of $Si_{75}H_{64}$ QD with the B3LYP functional take about 1.6 h on 16 processors, while the ML approach requires about 1 s for KS Hamiltonian construction and another 1 s for the Hamiltonian diagonalization. In this example, computing the atomic-guess Hamiltonian that is used as the input to the ML model takes even longer time, about 5.7 s on 16 processors (Table S1).

Table 1. Average Speed-Up of the Trained ML Models Compared with Typical SCF Calculations

		speed-up		
system	the atomic basis set size	PBE	B3LYP	HSE06
C_{60}	240	×37	×225	×217
$Si_{75}H_{64}$	1039	×16	×724	×435

Our acceleration approach lies merely in using the ML model as a one-shot KS Hamiltonian generation method. Viewed in this way, it can be regarded as a system-specific tight-binding or semiempirical method, made to reproduce the DFT calculation at a selected level of theory. Alternatively, one can regard the current approach as an improved guess for conventional electronic structure calculations, to yield the desired level of convergence on Hamiltonian matrix element errors (Section S5 in the Supporting Information, Figure S6). However, used in this way, one gets an acceleration factor of about 1.5−2, compared to the computational time of the SCF procedure that starts with the conventional charge density guess as a superposition of the atomic densities. As shown above, the current "one-shot" approach delivers a reasonable quality of the properties needed in NA-MD simulations. Thus, considering the sizable speed-up factors when it is used in this mode, we favor using it in this specific way.

To demonstrate the applicability of the ML-based approach to NA-MD simulations, we first compute the KS energy levels for every nuclear geometry sampled by the initial MD. The general agreement of the orbital energies computed for each system with the ML model to those obtained in conventional calculations (Figure 3a,b) suggests that the ML model can act as a successful yet much cheaper method to generate the surrogate Hamiltonians. As the ultimate test of the applicability of the ML-based approach to modeling NA-MD dynamics, we conduct such calculations using orbitals and orbital energies computed with the ML-based and conventional methods (details in Section S6 in the Supporting Information). Specifically, we compute the kinetics of excitation energy excess decay in both C_{60} and $Si_{75}H_{64}$ by using three trajectory surface hopping (TSH) methods: FSSH, ID-A, and mSDM (Figure 3c,d). As explained in the methodology section, the current calculations are conducted using a basis of single-particle states formulated as excited Slater determinants (Figures S1 and S2). Out of the TSH methods, the FSSH method is known to be prone to the overcoherence problem, while the ID-A and mSDM methods both introduce decoherence corrections to it. Our focus is primarily on the

https://doi.org/10.1021/acs.jctc.4c00008
J. Chem. Theory Comput. 2024, 20, 2992−3007

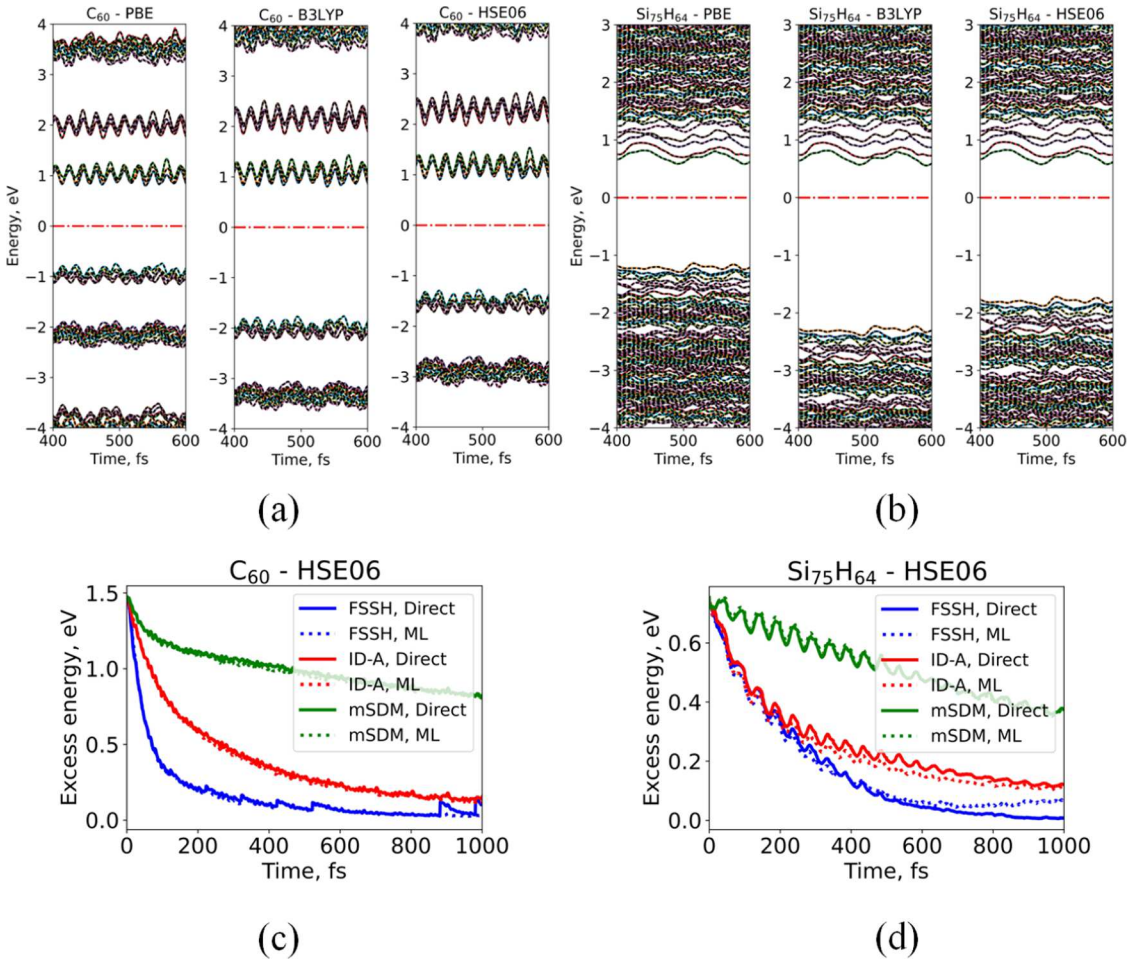

Figure 3. Applicability of the ML-based Hamiltonian in the NA-MD simulations: (a, b) reproducing single-particle orbital energies as functions of time for (a) C_{60} and (b) $Si_{75}H_{64}$ QD systems using ML models trained with data obtained with the PBE, B3LYP, and HSE06 functionals. The reference and ML MOs are shown with solid black and colored dotted lines, respectively. The Fermi energy level is shown by red dashed dotted line and set to zero. For better visualization, only a trajectory interval of 200 fs is shown. (c, d) Average excess energy decay obtained from NA-MD calculations using the FSSH, ID-A, and mSDM methods for (c) C_{60} and (d) $Si_{75}H_{64}$ QD systems with the calculations based on the HSE06 functional (solid lines) and the corresponding ML model (dotted lines).

usability of the ML-based approach for NA-MD simulations, so the particular choice of the approximations and methods is not important as long as the ML-based method agrees with the reference calculations based on the conventional approach.

The rate and degree of convergence of the relaxation time scales computed with the ML-based dynamics toward the reference values obtained using the conventional approach depends on the target density functional, the system, and the NA-MD methodology in which it is to be used (Figures 4 and S7−S12). Generally, only a small number of trajectory data points are needed to achieve such a convergence. For instance, for the C_{60} system, only 50 geometries are needed to achieve the convergence of the computed relaxation time scales for all of the target functionals. This fast convergence can be attributed to the high symmetry of the C_{60} molecule and its vibrations. Indeed, for the much less symmetric $Si_{75}H_{64}$ QD system, 250 geometries are needed to achieve the convergence of the NA-MD results with the target PBE functional; about 750 geometries are needed for tighter convergence of the energy relaxation curves with the HSE06 and B3LYP target functionals. A larger number of training data points is required with the target hybrid functionals than with the PBE one since the converged orbitals/KS Hamiltonian of the former ones are more distant from the orbitals/KS Hamiltonian obtained with the guess charge density and the PBE functional. For the $Si_{75}H_{64}$ QD system, we observe that it is harder to train the ML model of surrogate Hamiltonians with the B3LYP or HSE06 functionals than those with the target PBE functional. Finally, we find that it may need a larger number of training data points to converge the time scales computed by the mSDM method than for calculations with the ID-A or FSSH methods. This is because the mSDM requires knowing the pure dephasing rates, which are computed from the energy gap fluctuation. This means a higher accuracy of the energy gaps is required to obtain more accurate energy gap fluctuations. Yet, the ML models constructed are still capable of achieving such a challenging goal.

The deviations of the relaxation time scales for the Si QD system computed with the ML approach from the corresponding time scales obtained via the direct simulations (Figure 4d−f) could be attributed to various factors such as the level of regularization or convergence thresholds in training the corresponding ML models. However, the fact that such deviations are observed primarily for the FSSH method and not for the ID-A or mSDM methods (weaker deviations for the ID-A and a steady convergence toward the time scales from

https://doi.org/10.1021/acs.jctc.4c00008
J. Chem. Theory Comput. 2024, 20, 2992−3007

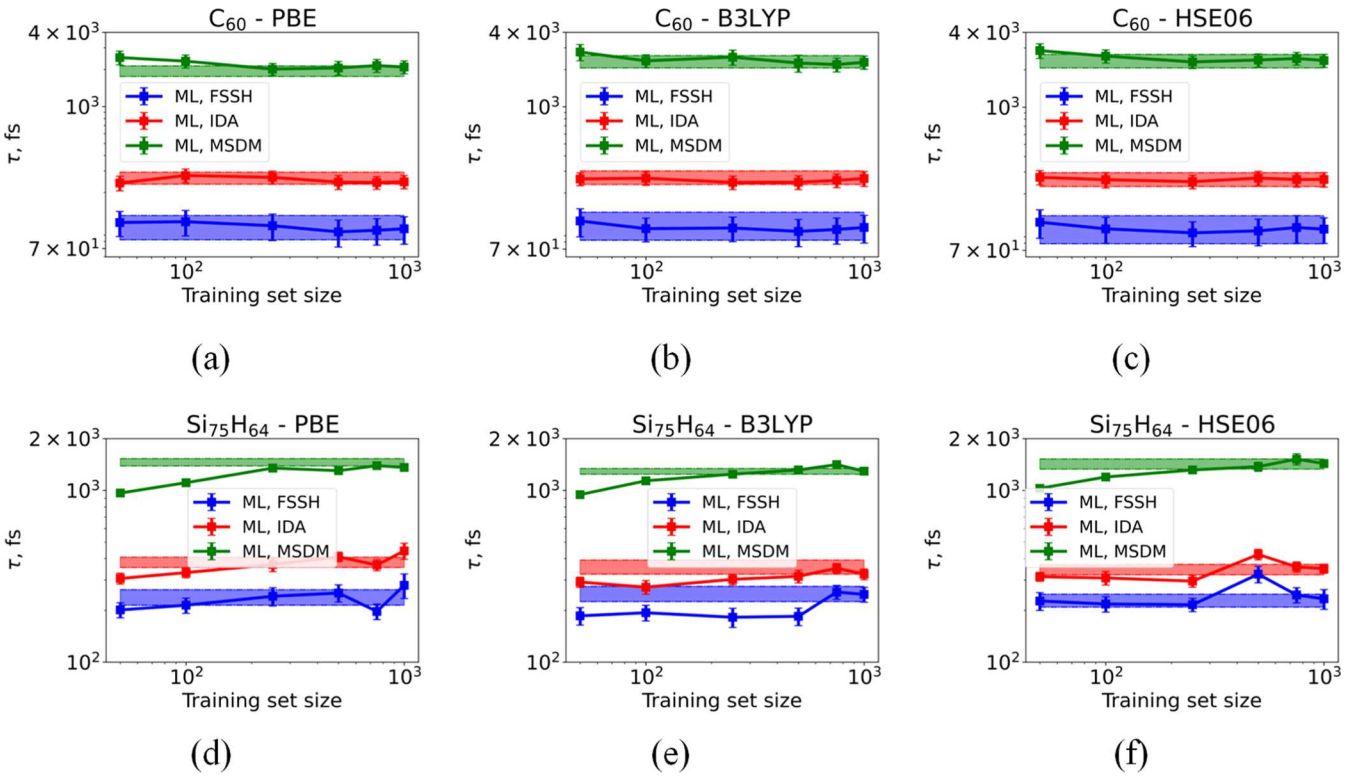

Figure 4. Relaxation time scales obtained from fitting the excess energy decay to the stretched−compressed exponential function, eq 17 for the (a−c) C_{60} and (d−f) $Si_{75}H_{64}$ QD structures for the (a, d) PBE, (b, e) B3LYP, and (c, f) HSE06 functionals. The time scales obtained from the dynamics in the ML basis are shown with solid lines. The colored areas show the average time scales and the corresponding confidence interval for the energy relaxation time scales computed with the conventional approach.

direct simulations for mSDM) suggests that the deviations are not necessarily indicative of the ML model quality. Furthermore, the deviations are observed mainly for the Si QD system (Figure 4d−f) and not for the C_{60} one (Figure 4a−c). The former has a density of states significantly higher than that of the latter (Figures 3a,b and S2). As Figure 2 shows, the accuracy of the orbitals themselves and their energies monotonically increases with respect to the number of points used to train the ML model. Thus, the nonmonotonic deviation of the computed time scales from the reference values does not originate from the absolute errors of the orbitals or their energies (quality of the ML model). What is remarkable about the Si QD system is its high density of states. In this situation, when dozens of states span a few eV or sub-eV intervals, small inaccuracies of states (orbitals) energies and time-overlaps still present in the ML model may cause multiple alternative scenarios for state crossings and trivial crossings. The state energies obtained from the ML model may still be rather close to the target values, but their ordering may be different from that of the reference state energies. Such small discrepancies may accumulate over time and eventually cause the divergence of the ML-based population dynamics from the reference one (e.g., longer time limit of blue curves in Figure 3d). In addition, due to close energy spacing, thermal excitations are possible within this manifold, increasing the effect of missed trivial crossing. This is where small energy level offsets (as predicted by the ML model) may lead to notable differences in the overall population dynamics. The effects are expected to be more pronounced for faster dynamics.

In the C_{60} system, the trivial crossings are likely to be better captured with the ML approach due to the lower density of states in this system. The time scale deviations are strongly pronounced in the FSSH dynamics compared to the ID-A (weak effect) or mSDM (almost no irregular deviations) cases. This trend can be explained by the faster overall dynamics: the methods that introduce decoherence corrections usually slow down the dynamics. The stronger they slow it down, the fewer potential trivial crossing events occur in the dynamics, leading to smaller deviations of the computed time scales from the reference values. Indeed, the deviation decays in order FSSH > ID-A > mSDM. To recapitulate the observations, we expect that the present ML-NAMD approach shall be more accurate for systems with lower densities of states, slower intrinsic dynamics, and when used with methods that introduce decoherence corrections. If one anticipates its use to larger systems with high densities of states and faster intrinsic dynamics, a higher care must be exercised (e.g., higher convergence thresholds or advanced regularization approaches) when constructing the corresponding ML models.

Our comprehensive calculations conducted with various reference density functionals and surface hopping methods and for each system are also summarized in Table 2 with the corresponding energy relaxation curves shown in Section S6 in the Supporting Information. Both Figure 4 and Table 2 demonstrate that for all kinds of calculations, the results of the ML-based dynamics match those from the conventional dynamics within the margins of error. Yet, the ML-based calculations are several orders of magnitude faster, both due to the one-shot philosophy and the need to use only a subset of geometries for ML construction, after which the computationally efficient ML model can replace the expensive direct electronic structure calculations for an indefinite number of

https://doi.org/10.1021/acs.jctc.4c00008
J. Chem. Theory Comput. 2024, 20, 2992−3007

Table 2. Excitation Energy Excess Relaxation Time Scales Obtained from Fitting the NA-MD Results by a Stretched−Compressed Exponential Function of $E(t) = E_0 \exp\left(-\left(\frac{t}{\tau}\right)^{\beta}\right)$[a]

		conventional (reference)		ML		
system	method	τ (fs)	β	τ (fs)	β	reference data
C_{60}	FSSH	PBE: 106 ± 24	PBE: 1.08 ± 0.09	PBE: 107 ± 26	PBE: 1.09 ± 0.10	<1 ps, 5.0 eV (exp.)[153]
		B3LYP: 111 ± 28	B3LYP: 1.13 ± 0.15	B3LYP: 104 ± 23	B3LYP: 1.19 ± 0.13	
		HSE06: 106 ± 27	HSE06: 1.19 ± 0.15	HSE06: 97 ± 22	HSE06: 1.13 ± 0.11	
	ID-A	PBE: 263 ± 30	PBE: 0.78 ± 0.06	PBE: 266 ± 33	PBE: 0.77 ± 0.07	
		B3LYP: 268 ± 34	B3LYP: 0.76 ± 0.07	B3LYP: 243 ± 30	B3LYP: 0.75 ± 0.07	
		HSE06: 263 ± 33	HSE06: 0.78 ± 0.07	HSE06: 251 ± 31	HSE06: 0.77 ± 0.06	
	mSDM	PBE: 1942 ± 195	PBE: 0.79 ± 0.14	PBE: 2012 ± 226	PBE: 0.78 ± 0.14	
		B3LYP: 2327 ± 267	B3LYP: 0.75 ± 0.13	B3LYP: 2518 ± 355	B3LYP: 0.76 ± 0.15	
		HSE06: 2361 ± 294	HSE06: 0.79 ± 0.16	HSE06: 2311 ± 270	HSE06: 0.76 ± 0.14	
$Si_{75}H_{64}$ (~1.4 nm)	FSSH	PBE: 237 ± 24	PBE: 0.67 ± 0.06	PBE: 241 ± 30	PBE: 0.74 ± 0.07	2−4 nm, 600 fs, 0.45−0.9 eV (exp.)[154]
		B3LYP: 250 ± 26	B3LYP: 0.74 ± 0.06	B3LYP: 182 ± 23	B3LYP: 0.57 ± 0.02	
		HSE06: 228 ± 20	HSE06: 1.09 ± 0.13	HSE06: 216 ± 19	HSE06: 0.95 ± 0.15	
	ID-A	PBE: 377 ± 26	PBE: 0.57 ± 0.03	PBE: 370 ± 34	PBE: 0.58 ± 0.08	1.2 nm, 102−170 fs, 1.0 eV (xTB calculations)[109]
		B3LYP: 362 ± 34	B3LYP: 0.62 ± 0.04	B3LYP: 302 ± 22	B3LYP: 0.57 ± 0.02	
		HSE06: 346 ± 24	HSE06: 0.67 ± 0.04	HSE06: 296 ± 23	HSE06: 0.65 ± 0.04	
	mSDM	PBE: 1431 ± 70	PBE: 1.09 ± 0.13	PBE: 1347 ± 71	PBE: 1.07 ± 0.12	1.5 nm, 400 fs, 1.0 eV (Landau−Zener calculations)[121]
		B3LYP: 1309 ± 54	B3LYP: 1.04 ± 0.12	B3LYP: 1241 ± 54	B3LYP: 0.98 ± 0.10	
		HSE06: 1425 ± 96	HSE06: 1.00 ± 0.13	HSE06: 1313 ± 52	HSE06: 1.09 ± 0.13	

[a]Experimental and previous computational time scales with QD size and initial excitation energy are shown.

molecular dynamics steps at a moderate expense of constructing the initial guess Hamiltonian for each geometry and the costs of electronic structure calculations needed for the ML training. The computational acceleration provided by the ML approach increases with the length of dynamical simulation and number of independent trajectories provided that the training set is representative of the configurational space to be explored by the NBRA NA-MD.

Although the main idea of this work is to validate the ML-based NA-MD approach, it is also instructive to discuss the time scales obtained, as well as the trends observed. First, we find that for both systems, the FSSH yields the fastest relaxation rate—about 100 fs for the C_{60} and 180−250 fs for the $Si_{75}H_{64}$ QD, while the ID-A yields a factor of 1.5−2 slower dynamics 240−270 fs for the C_{60} and 300−370 fs for the $Si_{75}H_{64}$ QD. Finally, the mSDM approach yields an order of magnitude slower dynamics compared to the FSSH—1.9−2.5 ps for the C_{60} and 1.2−1.4 ps for the $Si_{75}H_{64}$ QD.

The time scales obtained for C_{60} with the FSSH and ID-A methods fall within the known range of energy relaxation time scales for this system—less than 1 ps (Table 2), although the experimental result shown in Table 2 corresponds to relaxation of the bright excited states at about 5 eV. In this present setup, the calculations are done starting from a lower excited state at about 1.5 eV level. Thus, one can expect a slower relaxation time scale. The mSDM approach yields 1.9−2.5 ps, which appears to be a reasonable estimate of such a time scale since accounting for limitations of the current approach would make these numbers smaller, bringing them closer to the experimental results. Indeed, the NBRA approach presented here disregards possible nuclear reorganization in the excited states. Such a reorganization can lead the system to configurations with smaller energy gaps and hence larger NA couplings, if not directly to the conical intersection regions, leading to faster NA dynamics compared to what is possible within the NBRA treatment. Thus, the time scales reported in this work should be regarded as the upper limit to the true values, which are expected to be smaller. In addition to the better apparent agreement of the time scales, the estimate given by the current mSDM approach is likely to be more trustworthy since it accounts for important decoherence effects, which are not included within the FSSH approach. The 100 fs time scale given by the FSSH within the NBRA approach is expected to further decrease when the back-reaction effects are included. However, it is not expected to decrease too dramatically, since the nuclear reorganization effects themselves would occur on the comparable time scales of a few dozens of femtoseconds.

For the $Si_{75}H_{64}$ QD, the comparison with the reference data is more complicated due to a wide variety of such data and the variability of conditions and systems studied in these reference works. In the present work, we consider a 1.4 nm Si QD with an initial excess excitation energy of about 0.7 eV. Out of reference data shown in Table 2, the closed system studied experimentally could by the 2−4 nm QDs studied by Cimpean et al.[154] For the initial excess excitation energy of 0.45−0.9 eV,

https://doi.org/10.1021/acs.jctc.4c00008
J. Chem. Theory Comput. 2024, 20, 2992−3007

their results suggest about 600 fs relaxation time scales. Our previous calculations with the xTB single-particle states suggested the 102 fs (FSSH), 170 fs (ID-A), and 144 fs (mSDM) time scales for a comparable 1.2 nm Si QD.[109] The present values for the FSSH (220−250 fs) and ID-A (350−380 fs) are larger than the corresponding xTB-based values by a factor of 2, due to larger energy gaps yielded by DFT functionals (present work) in comparison to those of the xTB.[109] The present mSDM time scale (1.3−1.4 ps) is much larger than the one reported with the xTB approach, possibly due to smaller dephasing times in the current approach (as correlates with the larger energy gaps than in the xTB). The prior calculations by Reeves et al. on 1.5 nm QDs with initial excess excitation energy of 1.0 eV yielded 400 fs,[155] while the Landau−Zener calculations of Smith and Akimov based on TD-DFTB Hamiltonian suggested 182 fs for a comparably sized system.[121] Overall, the 350−380 fs yielded by the ID-A appears to be in the best agreement with the previously reported data. However, we believe the 1.3−1.4 ps predicted by the mSDM should be regarded as better estimates for the level of theory used. Compared to the experimental values, this number is somewhat overestimated; however, bringing in other effects such as back-reaction and many-body nature of excited states would decrease these numbers, bringing them closer to the experimental results. Similar to the C_{60} example discussed above, the present time scales should be regarded as the upper limits—going beyond the NBRA may lead to a faster dynamics.[104] Indeed, allowing the nuclei to evolve on excited state PES within the non-NBRA approach is likely to lead them to the regions of stronger nonadiabatic couplings or find conical intersections as opposed to the nuclear dynamics governed by the ground state PES. In the latter case, the nuclei may be evolving in the configurational space regions that are far from the strong NA coupling/conical intersection regions. Hence, the NBRA dynamics are likely to yield underestimated relaxation rates.

As just mentioned, the present simulations for both systems are conducted with the basis of excited Slater determinants and hence are intrinsically single-particle in nature. Extending the calculations to the many-body states is likely to accelerate the corresponding excess excitation energy relaxation process,[23] lowering the current predictions (especially for the mSDM) and bringing them in closer agreement with the experiment.

4. CONCLUSIONS

In this work, we present a new ML-based KS Hamiltonian mapping approach for nonadiabatic molecular dynamics. The method allows one to map an easily computed non-self-consistent KS Hamiltonian with the charge density given by the superposition of atomic densities and a chosen density functional to a nearly converged (self-consistent) KS Hamiltonian constructed using alternative, potentially more accurate and expensive (e.g., hybrid), functionals. We demonstrate that a simple linear kernel ridge regression ML model can be used to realize such a mapping. Only a few hundred geometries are needed to achieve satisfactory accuracy of the trained ML model. The resulting model enables the acceleration of the NBRA-based NA-MD simulations by several orders of magnitude.

As a demonstration, we compute the excitation energy excess relaxation dynamics in a C_{60} molecule and a 1.4 nm Si QD using the ML-mapped KS Hamiltonians corresponding to hybrid functionals such as the B3LYP or HSE06. For the C_{60}, the 1.5 eV excess excitation energy relaxes with the time scales of 100 fs (FSSH), 240−270 fs (ID-A), and 1.9−2.5 ps (mSDM). For the $Si_{75}H_{64}$ QD, the 0.7 eV excess excitation energy relaxes with the time scales of 180−250 fs (FSSH), 350−380 fs (ID-A), and 1.3−1.4 ps (mSDM). We suggest these time scales to be regarded as the upper limits of the true values, since the present numbers do not account for possible many-body effects and nuclear reorganization of systems in excited states. Considering such limits, the present results are in good agreement with the reported experimental findings.

We find that the ML-based NA dynamics is in good agreement with the conventional NA-MD results. For all systems and functionals, we find that the time scales are related as $\tau_{FSSH} < \tau_{ID\text{-}A} < \tau_{mSDM}$. The deviations of the time scales computed with the ML-NA-MD approach from the corresponding reference values decrease for systems with lower density of states and slower intrinsic dynamics as well as when using it with the TSH methods that account for decoherence effects and hence produce slower relaxation dynamics. We note that the method may require more care when applied to larger systems with high densities of states and fast intrinsic dynamics. Furthermore, for all systems, we observe only a weak dependence of the computed time scales on the target (reproduced by the ML model) functional. Surprisingly, the computed time scales are similar whether the PBE, B3LYP, or HSE06 functionals are used.

■ ASSOCIATED CONTENT

Supporting Information

The Supporting Information is available free of charge at https://pubs.acs.org/doi/10.1021/acs.jctc.4c00008.

Time-dependent KS and Slater determinant energies, densities of states, discussion of KS Hamiltonian matrix partitioning strategies, convergence data for ML models, ML and electronic structure timing data, data on SCF convergence when started with the ML-based guess, details of excitation energy excess relaxation dynamics for all methods, systems, and models, detailed scripts, and input files used for all types of calculations available in digital form online at Zenodo server[149] (PDF)

■ AUTHOR INFORMATION

Corresponding Author

Alexey V. Akimov − *Department of Chemistry, University at Buffalo, The State University of New York, Buffalo, New York 14260, United States;* orcid.org/0000-0002-7815-3731; Email: alexeyak@buffalo.edu, @AkimovLab

Author

Mohammad Shakiba − *Department of Chemistry, University at Buffalo, The State University of New York, Buffalo, New York 14260, United States*

Complete contact information is available at: https://pubs.acs.org/10.1021/acs.jctc.4c00008

Notes

The authors declare no competing financial interest.

■ ACKNOWLEDGMENTS

The authors acknowledge the financial support of the National Science Foundation (Grant NSF-2045204). Support of

computations was provided by the Center for Computational Research at the University at Buffalo.

REFERENCES

(1) Melnychuk, C.; Guyot-Sionnest, P. Multicarrier Dynamics in Quantum Dots. *Chem. Rev.* **2021**, *121*, 2325−2372.
(2) Nozik, A. J.; Beard, M. C.; Luther, J. M.; Law, M.; Ellingson, R. J.; Johnson, J. C. Semiconductor Quantum Dots and Quantum Dot Arrays and Applications of Multiple Exciton Generation to Third-Generation Photovoltaic Solar Cells. *Chem. Rev.* **2010**, *110*, 6873−6890.
(3) Protesescu, L.; Yakunin, S.; Bodnarchuk, M. I.; Krieg, F.; Caputo, R.; Hendon, C. H.; Yang, R. X.; Walsh, A.; Kovalenko, M. V. Nanocrystals of Cesium Lead Halide Perovskites ($CsPbX_3$, X = Cl, Br, and I): Novel Optoelectronic Materials Showing Bright Emission with Wide Color Gamut. *Nano Lett.* **2015**, *15*, 3692−3696.
(4) Guerrero, A.; Bisquert, J.; Garcia-Belmonte, G. Impedance Spectroscopy of Metal Halide Perovskite Solar Cells from the Perspective of Equivalent Circuits. *Chem. Rev.* **2021**, *121*, 14430−14484.
(5) Kim, J. Y.; Lee, J.-W.; Jung, H. S.; Shin, H.; Park, N.-G. High-Efficiency Perovskite Solar Cells. *Chem. Rev.* **2020**, *120*, 7867−7918.
(6) Snaith, H. J. Perovskites: The Emergence of a New Era for Low-Cost, High-Efficiency Solar Cells. *J. Phys. Chem. Lett.* **2013**, *4*, 3623−3630.
(7) Chen, B.; N Rudd, P.; Yang, S.; Yuan, Y.; Huang, J. Imperfections and Their Passivation in Halide Perovskite Solar Cells. *Chem. Soc. Rev.* **2019**, *48*, 3842−3867.
(8) He, X.; Htoon, H.; Doorn, S. K.; Pernice, W. H. P.; Pyatkov, F.; Krupke, R.; Jeantet, A.; Chassagneux, Y.; Voisin, C. Carbon Nanotubes as Emerging Quantum-Light Sources. *Nat. Mater.* **2018**, *17*, 663−670.
(9) He, X.; Hartmann, N. F.; Ma, X.; Kim, Y.; Ihly, R.; Blackburn, J. L.; Gao, W.; Kono, J.; Yomogida, Y.; Hirano, A.; Tanaka, T.; Kataura, H.; Htoon, H.; Doorn, S. K. Tunable Room-Temperature Single-Photon Emission at Telecom Wavelengths from Sp3 Defects in Carbon Nanotubes. *Nat. Photonics* **2017**, *11*, 577−582.
(10) Zhu, L.; Zhang, M.; Xu, J.; Li, C.; Yan, J.; Zhou, G.; Zhong, W.; Hao, T.; Song, J.; Xue, X.; Zhou, Z.; Zeng, R.; Zhu, H.; Chen, C.-C.; MacKenzie, R. C. I.; Zou, Y.; Nelson, J.; Zhang, Y.; Sun, Y.; Liu, F. Single-Junction Organic Solar Cells with over 19% Efficiency Enabled by a Refined Double-Fibril Network Morphology. *Nat. Mater.* **2022**, *21*, 656−663.
(11) Xu, X.; Jing, W.; Meng, H.; Guo, Y.; Yu, L.; Li, R.; Peng, Q. Sequential Deposition of Multicomponent Bulk Heterojunctions Increases Efficiency of Organic Solar Cells. *Adv. Mater.* **2023**, *35*, No. 2208997.
(12) Shockley, W.; Queisser, H. J. Detailed Balance Limit of Efficiency of P-n Junction Solar Cells. *J. Appl. Phys.* **1961**, *32*, 510−519.
(13) Akimov, A. V.; Prezhdo, O. V. Nonadiabatic Dynamics of Charge Transfer and Singlet Fission at the Pentacene/C_{60} Interface. *J. Am. Chem. Soc.* **2014**, *136*, 1599−1608.
(14) Grimaldi, G.; Crisp, R. W.; ten Brinck, S.; Zapata, F.; van Ouwendorp, M.; Renaud, N.; Kirkwood, N.; Evers, W. H.; Kinge, S.; Infante, I.; Siebbeles, L. D. A.; Houtepen, A. J. Hot-Electron Transfer in Quantum-Dot Heterojunction Films. *Nat. Commun.* **2018**, *9*, No. 2310.
(15) Chu, W.; Tan, S.; Zheng, Q.; Fang, W.; Feng, Y.; Prezhdo, O. V.; Wang, B.; Li, X.-Z.; Zhao, J. Ultrafast Charge Transfer Coupled to Quantum Proton Motion at Molecule/Metal Oxide Interface. *Sci. Adv.* **2022**, *8*, No. eabo2675.
(16) Long, R.; English, N. J.; Prezhdo, O. V. Defects Are Needed for Fast Photo-Induced Electron Transfer from a Nanocrystal to a Molecule: Time-Domain *Ab Initio* Analysis. *J. Am. Chem. Soc.* **2013**, *135*, 18892−18900.
(17) Long, R.; Liu, J.; Prezhdo, O. V. Unravelling the Effects of Grain Boundary and Chemical Doping on Electron−Hole Recombination in $CH_3NH_3PbI_3$ Perovskite by Time-Domain Atomistic Simulation. *J. Am. Chem. Soc.* **2016**, *138*, 3884−3890.
(18) Li, W.; Sun, Y.-Y.; Li, L.; Zhou, Z.; Tang, J.; Prezhdo, O. V. Control of Charge Recombination in Perovskites by Oxidation State of Halide Vacancy. *J. Am. Chem. Soc.* **2018**, *140*, 15753−15763.
(19) Tong, C.-J.; Cai, X.; Zhu, A.-Y.; Liu, L.-M.; Prezhdo, O. V. How Hole Injection Accelerates Both Ion Migration and Nonradiative Recombination in Metal Halide Perovskites. *J. Am. Chem. Soc.* **2022**, *144*, 6604−6612.
(20) Li, L.; Long, R.; Bertolini, T.; Prezhdo, O. V. Sulfur Adatom and Vacancy Accelerate Charge Recombination in MoS_2 but by Different Mechanisms: Time-Domain Ab Initio Analysis. *Nano Lett.* **2017**, *17*, 7962−7967.
(21) Shakiba, M.; Akimov, A. V. Dependence of Electron−Hole Recombination Rates on Charge Carrier Concentration: A Case Study of Nonadiabatic Molecular Dynamics in Graphitic Carbon Nitride Monolayers. *J. Phys. Chem. C* **2023**, *127*, 9083−9096.
(22) Zhou, Z.; He, J.; Frauenheim, T.; Prezhdo, O. V.; Wang, J. Control of Hot Carrier Cooling in Lead Halide Perovskites by Point Defects. *J. Am. Chem. Soc.* **2022**, *144*, 18126−18134.
(23) Smith, B.; Shakiba, M.; Akimov, A. V. Nonadiabatic Dynamics in Si and CdSe Nanoclusters: Many-Body vs Single-Particle Treatment of Excited States. *J. Chem. Theory Comput.* **2021**, *17*, 678−693.
(24) Smith, B.; Shakiba, M.; Akimov, A. V. Crystal Symmetry and Static Electron Correlation Greatly Accelerate Nonradiative Dynamics in Lead Halide Perovskites. *J. Phys. Chem. Lett.* **2021**, *12*, 2444−2453.
(25) Zhang, J.; Hong, H.; Zhang, J.; Fu, H.; You, P.; Lischner, J.; Liu, K.; Kaxiras, E.; Meng, S. New Pathway for Hot Electron Relaxation in Two-Dimensional Heterostructures. *Nano Lett.* **2018**, *18*, 6057−6063.
(26) Akimov, A. V.; Asahi, R.; Jinnouchi, R.; Prezhdo, O. V. What Makes the Photocatalytic CO $_2$ Reduction on N-Doped Ta_2O_5 Efficient: Insights from Nonadiabatic Molecular Dynamics. *J. Am. Chem. Soc.* **2015**, *137*, 11517−11525.
(27) Akimov, A. V.; Jinnouchi, R.; Shirai, S.; Asahi, R.; Prezhdo, O. V. Theoretical Insights into the Impact of Ru Catalyst Anchors on the Efficiency of Photocatalytic CO_2 Reduction on Ta_2O_5. *J. Phys. Chem. B* **2015**, *119*, 7186−7197.
(28) Cheng, C.; Fang, W.-H.; Long, R.; Prezhdo, O. V. Water Splitting with a Single-Atom Cu/TiO2 Photocatalyst: Atomistic Origin of High Efficiency and Proposed Enhancement by Spin Selection. *JACS Au* **2021**, *1*, 550−559.
(29) Niu, X.; Bai, X.; Zhou, Z.; Wang, J. Rational Design and Characterization of Direct Z-Scheme Photocatalyst for Overall Water Splitting from Excited State Dynamics Simulations. *ACS Catal.* **2020**, *10*, 1976−1983.
(30) Nelson, T. R.; White, A. J.; Bjorgaard, J. A.; Sifain, A. E.; Zhang, Y.; Nebgen, B.; Fernandez-Alberti, S.; Mozyrsky, D.; Roitberg, A. E.; Tretiak, S. Non-Adiabatic Excited-State Molecular Dynamics: Theory and Applications for Modeling Photophysics in Extended Molecular Materials. *Chem. Rev.* **2020**, *120*, 2215−2287.
(31) Curchod, B. F. E.; Martínez, T. J. Ab Initio Nonadiabatic Quantum Molecular Dynamics. *Chem. Rev.* **2018**, *118*, 3305−3336.
(32) Perdew, J. P.; Burke, K.; Ernzerhof, M. Generalized Gradient Approximation Made Simple. *Phys. Rev. Lett.* **1996**, *77*, 3865−3868.
(33) Lin, Y.; Akimov, A. V. Dependence of Nonadiabatic Couplings with Kohn−Sham Orbitals on the Choice of Density Functional: Pure vs Hybrid. *J. Phys. Chem. A* **2016**, *120*, 9028−9041.
(34) Vamathevan, J.; Clark, D.; Czodrowski, P.; Dunham, I.; Ferran, E.; Lee, G.; Li, B.; Madabhushi, A.; Shah, P.; Spitzer, M.; Zhao, S. Applications of Machine Learning in Drug Discovery and Development. *Nat. Rev. Drug Discovery* **2019**, *18*, 463−477.
(35) von Lilienfeld, O. A.; Müller, K.-R.; Tkatchenko, A. Exploring Chemical Compound Space with Quantum-Based Machine Learning. *Nat. Rev. Chem.* **2020**, *4*, 347−358.
(36) Mai, H.; Le, T. C.; Chen, D.; Winkler, D. A.; Caruso, R. A. Machine Learning for Electrocatalyst and Photocatalyst Design and Discovery. *Chem. Rev.* **2022**, *122*, 13478−13515.

https://doi.org/10.1021/acs.jctc.4c00008
J. Chem. Theory Comput. 2024, 20, 2992−3007

(37) Meuwly, M. Machine Learning for Chemical Reactions. *Chem. Rev.* **2021**, *121*, 10218−10239.
(38) Huang, S.-D.; Shang, C.; Kang, P.-L.; Zhang, X.-J.; Liu, Z.-P. LASP: Fast Global Potential Energy Surface Exploration. *Wiley Interdiscip. Rev.: Comput. Mol. Sci.* **2019**, *9*, No. e1415.
(39) Stocker, S.; Csányi, G.; Reuter, K.; Margraf, J. T. Machine Learning in Chemical Reaction Space. *Nat. Commun.* **2020**, *11*, No. 5505.
(40) Zeng, J.; Cao, L.; Xu, M.; Zhu, T.; Zhang, J. Z. H. Complex Reaction Processes in Combustion Unraveled by Neural Network-Based Molecular Dynamics Simulation. *Nat. Commun.* **2020**, *11*, No. 5713.
(41) Ben Mahmoud, C.; Anelli, A.; Csányi, G.; Ceriotti, M. Learning the Electronic Density of States in Condensed Matter. *Phys. Rev. B* **2020**, *102*, No. 235130.
(42) Zhang, Z.; Zhang, Y.; Wang, J.; Xu, J.; Long, R. Doping-Induced Charge Localization Suppresses Electron−Hole Recombination in Copper Zinc Tin Sulfide: Quantum Dynamics Combined with Deep Neural Networks Analysis. *J. Phys. Chem. Lett.* **2021**, *12*, 835−842.
(43) Guan, Y.; Yarkony, D. R. Accurate Neural Network Representation of the Ab Initio Determined Spin−Orbit Interaction in the Diabatic Representation Including the Effects of Conical Intersections. *J. Phys. Chem. Lett.* **2020**, *11*, 1848−1858.
(44) Unke, O. T.; Chmiela, S.; Sauceda, H. E.; Gastegger, M.; Poltavsky, I.; Schütt, K. T.; Tkatchenko, A.; Müller, K.-R. Machine Learning Force Fields. *Chem. Rev.* **2021**, *121*, 10142−10186.
(45) Pinheiro, M.; Ge, F.; Ferré, N.; Dral, P. O.; Barbatti, M. Choosing the Right Molecular Machine Learning Potential. *Chem. Sci.* **2021**, *12*, 14396−14413.
(46) Ramakrishnan, R.; Dral, P. O.; Rupp, M.; von Lilienfeld, O. A. Big Data Meets Quantum Chemistry Approximations: The Δ-Machine Learning Approach. *J. Chem. Theory Comput.* **2015**, *11*, 2087−2096.
(47) Bowman, J. M.; Qu, C.; Conte, R.; Nandi, A.; Houston, P. L.; Yu, Q. Δ-Machine Learned Potential Energy Surfaces and Force Fields. *J. Chem. Theory Comput.* **2023**, *19*, 1−17.
(48) Tong, Q.; Gao, P.; Liu, H.; Xie, Y.; Lv, J.; Wang, Y.; Zhao, J. Combining Machine Learning Potential and Structure Prediction for Accelerated Materials Design and Discovery. *J. Phys. Chem. Lett.* **2020**, *11*, 8710−8720.
(49) Dral, P. O. Quantum Chemistry in the Age of Machine Learning. *J. Phys. Chem. Lett.* **2020**, *11*, 2336−2347.
(50) Zubatiuk, T.; Isayev, O. Development of Multimodal Machine Learning Potentials: Toward a Physics-Aware Artificial Intelligence. *Acc. Chem. Res.* **2021**, *54*, 1575−1585.
(51) Fedik, N.; Zubatyuk, R.; Kulichenko, M.; Lubbers, N.; Smith, J. S.; Nebgen, B.; Messerly, R.; Li, Y. W.; Boldyrev, A. I.; Barros, K.; Isayev, O.; Tretiak, S. Extending Machine Learning beyond Interatomic Potentials for Predicting Molecular Properties. *Nat. Rev. Chem.* **2022**, *6*, 653−672.
(52) Talapatra, A.; Uberuaga, B. P.; Stanek, C. R.; Pilania, G. Band Gap Predictions of Double Perovskite Oxides Using Machine Learning. *Commun. Mater.* **2023**, *4*, No. 46.
(53) Zhuo, Y.; Mansouri Tehrani, A.; Brgoch, J. Predicting the Band Gaps of Inorganic Solids by Machine Learning. *J. Phys. Chem. Lett.* **2018**, *9*, 1668−1673.
(54) Xue, B.-X.; Barbatti, M.; Dral, P. O. Machine Learning for Absorption Cross Sections. *J. Phys. Chem. A* **2020**, *124*, 7199−7210.
(55) Ullah, A.; Dral, P. O. Predicting the Future of Excitation Energy Transfer in Light-Harvesting Complex with Artificial Intelligence-Based Quantum Dynamics. *Nat. Commun.* **2022**, *13*, No. 1930.
(56) Westermayr, J.; Marquetand, P. Deep Learning for UV Absorption Spectra with SchNarc: First Steps toward Transferability in Chemical Compound Space. *J. Chem. Phys.* **2020**, *153*, No. 154112.
(57) Liu, F.; Du, L.; Zhang, D.; Gao, J. Direct Learning Hidden Excited State Interaction Patterns from Ab Initio Dynamics and Its Implication as Alternative Molecular Mechanism Models. *Sci. Rep.* **2017**, *7*, No. 8737.
(58) Keith, J. A.; Vassilev-Galindo, V.; Cheng, B.; Chmiela, S.; Gastegger, M.; Müller, K.-R.; Tkatchenko, A. Combining Machine Learning and Computational Chemistry for Predictive Insights Into Chemical Systems. *Chem. Rev.* **2021**, *121*, 9816−9872.
(59) Butler, K. T.; Davies, D. W.; Cartwright, H.; Isayev, O.; Walsh, A. Machine Learning for Molecular and Materials Science. *Nature* **2018**, *559*, 547−555.
(60) Shao, X.; Paetow, L.; Tuckerman, M. E.; Pavanello, M. Machine Learning Electronic Structure Methods Based on the One-Electron Reduced Density Matrix. *Nat. Commun.* **2023**, *14*, No. 6281.
(61) Wang, Z.; Dong, J.; Qiu, J.; Wang, L. All-Atom Nonadiabatic Dynamics Simulation of Hybrid Graphene Nanoribbons Based on Wannier Analysis and Machine Learning. *ACS Appl. Mater. Interfaces* **2022**, *14*, 22929−22940.
(62) Rodríguez, L. E. H.; Ullah, A.; Espinosa, K. J. R.; Dral, P. O.; Kananenka, A. A. A Comparative Study of Different Machine Learning Methods for Dissipative Quantum Dynamics. *Mach. Learn. Sci. Technol.* **2022**, *3*, No. 045016.
(63) Herrera Rodríguez, L. E.; Kananenka, A. A. Convolutional Neural Networks for Long Time Dissipative Quantum Dynamics. *J. Phys. Chem. Lett.* **2021**, *12*, 2476−2483.
(64) Ullah, A.; Dral, P. O. Speeding up Quantum Dissipative Dynamics of Open Systems with Kernel Methods. *New J. Phys.* **2021**, *23*, No. 113019.
(65) Ullah, A.; Dral, P. O. MLQD: A Package for Machine Learning-Based Quantum Dissipative Dynamics. *Comput. Phys. Commun.* **2024**, *294*, No. 108940.
(66) Dral, P. O.; Ge, F.; Hou, Y.-F.; Zheng, P.; Chen, Y.; Barbatti, M.; Isayev, O.; Wang, C.; Xue, B.-X.; Pinheiro, M., Jr; Su, Y.; Dai, Y.; Chen, Y.; Zhang, L.; Zhang, S.; Ullah, A.; Zhang, Q.; Ou, Y. MLatom 3: A Platform for Machine Learning-Enhanced Computational Chemistry Simulations and Workflows. *J. Chem. Theory Comput.* **2024**, *20*, 1193−1213.
(67) Akimov, A. V. Extending the Time Scales of Nonadiabatic Molecular Dynamics via Machine Learning in the Time Domain. *J. Phys. Chem. Lett.* **2021**, *12*, 12119−12128.
(68) Liu, D.; Wu, Y.; Vasenko, A. S.; Prezhdo, O. V. Grain Boundary Sliding and Distortion on a Nanosecond Timescale Induce Trap States in $CsPbBr_3$: Ab Initio Investigation with Machine Learning Force Field. *Nanoscale* **2022**, *15*, 285−293.
(69) Mangan, S. M.; Zhou, G.; Chu, W.; Prezhdo, O. V. Dependence between Structural and Electronic Properties of $CsPbI_3$: Unsupervised Machine Learning of Nonadiabatic Molecular Dynamics. *J. Phys. Chem. Lett.* **2021**, *12*, 8672−8678.
(70) Wang, B.; Chu, W.; Prezhdo, O. V. Interpolating Nonadiabatic Molecular Dynamics Hamiltonian with Inverse Fast Fourier Transform. *J. Phys. Chem. Lett.* **2022**, *13*, 331−338.
(71) Cignoni, E.; Cupellini, L.; Mennucci, B. Machine Learning Exciton Hamiltonians in Light-Harvesting Complexes. *J. Chem. Theory Comput.* **2023**, *19*, 965−977.
(72) Chandrasekaran, A.; Kamal, D.; Batra, R.; Kim, C.; Chen, L.; Ramprasad, R. Solving the Electronic Structure Problem with Machine Learning. *npj Comput. Mater.* **2019**, *5*, No. 22.
(73) Li, X.; Lubbers, N.; Tretiak, S.; Barros, K.; Zhang, Y. Machine Learning Framework for Modeling Exciton Polaritons in Molecular Materials. *J. Chem. Theory Comput.* **2024**, *20*, 891−901.
(74) Habib, A.; Lubbers, N.; Tretiak, S.; Nebgen, B. Machine Learning Models Capture Plasmon Dynamics in Ag Nanoparticles. *J. Phys. Chem. A* **2023**, *127*, 3768−3778.
(75) Westermayr, J.; Gastegger, M.; Marquetand, P. Combining SchNet and SHARC: The SchNarc Machine Learning Approach for Excited-State Dynamics. *J. Phys. Chem. Lett.* **2020**, *11*, 3828−3834.
(76) Schütt, K. T.; Sauceda, H. E.; Kindermans, P.-J.; Tkatchenko, A.; Müller, K.-R. SchNet − A Deep Learning Architecture for Molecules and Materials. *J. Chem. Phys.* **2018**, *148*, No. 241722.
(77) Schütt, K. T.; Kessel, P.; Gastegger, M.; Nicoli, K. A.; Tkatchenko, A.; Müller, K.-R. SchNetPack: A Deep Learning Toolbox For Atomistic Systems. *J. Chem. Theory Comput.* **2019**, *15*, 448−455.

https://doi.org/10.1021/acs.jctc.4c00008
J. Chem. Theory Comput. 2024, 20, 2992−3007

(78) Mai, S.; Marquetand, P.; González, L. Nonadiabatic Dynamics: The SHARC Approach. *Wiley Interdiscip. Rev.: Comput. Mol. Sci.* **2018**, *8*, No. e1370.
(79) Tully, J. C.; Preston, R. K. Trajectory Surface Hopping Approach to Nonadiabatic Molecular Collisions: The Reaction of H+ with D2. *J. Chem. Phys.* **1971**, *55* (2), 562−572.
(80) Tully, J. C. Molecular Dynamics with Electronic Transitions. *J. Chem. Phys.* **1990**, *93*, 1061−1071.
(81) Hu, D.; Xie, Y.; Li, X.; Li, L.; Lan, Z. Inclusion of Machine Learning Kernel Ridge Regression Potential Energy Surfaces in On-the-Fly Nonadiabatic Molecular Dynamics Simulation. *J. Phys. Chem. Lett.* **2018**, *9*, 2725−2732.
(82) Chen, W.-K.; Liu, X.-Y.; Fang, W.-H.; Dral, P. O.; Cui, G. Deep Learning for Nonadiabatic Excited-State Dynamics. *J. Phys. Chem. Lett.* **2018**, *9*, 6702−6708.
(83) Hu, F.; He, F.; Yaron, D. J. Treating Semiempirical Hamiltonians as Flexible Machine Learning Models Yields Accurate and Interpretable Results. *J. Chem. Theory Comput.* **2023**, *19*, 6185−6196.
(84) Zhou, G.; Lubbers, N.; Barros, K.; Tretiak, S.; Nebgen, B. Deep Learning of Dynamically Responsive Chemical Hamiltonians with Semiempirical Quantum Mechanics. *Proc. Natl. Acad. Sci. U.S.A.* **2022**, *119*, No. e2120333119.
(85) Christensen, A. S.; Sirumalla, S. K.; Qiao, Z.; O'Connor, M. B.; Smith, D. G. A.; Ding, F.; Bygrave, P. J.; Anandkumar, A.; Welborn, M.; Manby, F. R.; Miller, T. F., III OrbNet Denali: A Machine Learning Potential for Biological and Organic Chemistry with Semi-Empirical Cost and DFT Accuracy. *J. Chem. Phys.* **2021**, *155*, No. 204103.
(86) Ge, F.; Zhang, L.; Hou, Y.-F.; Chen, Y.; Ullah, A.; Dral, P. O. Four-Dimensional-Spacetime Atomistic Artificial Intelligence Models. *J. Phys. Chem. Lett.* **2023**, *14*, 7732−7743.
(87) Dral, P. O.; Barbatti, M.; Thiel, W. Nonadiabatic Excited-State Dynamics with Machine Learning. *J. Phys. Chem. Lett.* **2018**, *9*, 5660−5663.
(88) Denzel, A.; Kästner, J. Gaussian Process Regression for Transition State Search. *J. Chem. Theory Comput.* **2018**, *14*, 5777−5786.
(89) Denzel, A.; Kästner, J. Gaussian Process Regression for Geometry Optimization. *J. Chem. Phys.* **2018**, *148*, No. 094114.
(90) Galván, I. F.; Raggi, G.; Lindh, R. Restricted-Variance Constrained, Reaction Path, and Transition State Molecular Optimizations Using Gradient-Enhanced Kriging. *J. Chem. Theory Comput.* **2021**, *17*, 571−582.
(91) Schmitz, G.; Klinting, E. L.; Christiansen, O. A Gaussian Process Regression Adaptive Density Guided Approach for Potential Energy Surface Construction. *J. Chem. Phys.* **2020**, *153*, No. 064105.
(92) Raggi, G.; Galván, I. F.; Ritterhoff, C. L.; Vacher, M.; Lindh, R. Restricted-Variance Molecular Geometry Optimization Based on Gradient-Enhanced Kriging. *J. Chem. Theory Comput.* **2020**, *16*, 3989−4001.
(93) Häse, F.; Galván, I. F.; Aspuru-Guzik, A.; Lindh, R.; Vacher, M. How Machine Learning Can Assist the Interpretation of Ab Initio Molecular Dynamics Simulations and Conceptual Understanding of Chemistry. *Chem. Sci.* **2019**, *10*, 2298−2307.
(94) Schütt, K. T.; Gastegger, M.; Tkatchenko, A.; Müller, K.-R.; Maurer, R. J. Unifying Machine Learning and Quantum Chemistry with a Deep Neural Network for Molecular Wavefunctions. *Nat. Commun.* **2019**, *10*, No. 5024.
(95) Rupp, M.; Tkatchenko, A.; Müller, K.-R.; von Lilienfeld, O. A. Fast and Accurate Modeling of Molecular Atomization Energies with Machine Learning. *Phys. Rev. Lett.* **2012**, *108*, No. 058301.
(96) Chmiela, S.; Tkatchenko, A.; Sauceda, H. E.; Poltavsky, I.; Schütt, K. T.; Müller, K.-R. Machine Learning of Accurate Energy-Conserving Molecular Force Fields. *Sci. Adv.* **2017**, *3*, No. e1603015.
(97) Westermayr, J.; Gastegger, M.; Menger, M. F. S. J.; Mai, S.; González, L.; Marquetand, P. Machine Learning Enables Long Time Scale Molecular Photodynamics Simulations. *Chem. Sci.* **2019**, *10*, 8100−8107.
(98) Sonoda, S.; Murata, N. Neural Network with Unbounded Activation Functions Is Universal Approximator. *Appl. Comput. Harmonic Anal.* **2017**, *43*, 233−268.
(99) Hansen, K.; Biegler, F.; Ramakrishnan, R.; Pronobis, W.; von Lilienfeld, O. A.; Müller, K.-R.; Tkatchenko, A. Machine Learning Predictions of Molecular Properties: Accurate Many-Body Potentials and Nonlocality in Chemical Space. *J. Phys. Chem. Lett.* **2015**, *6*, 2326−2331.
(100) Dral, P. O.; Owens, A.; Yurchenko, S. N.; Thiel, W. Structure-Based Sampling and Self-Correcting Machine Learning for Accurate Calculations of Potential Energy Surfaces and Vibrational Levels. *J. Chem. Phys.* **2017**, *146*, No. 244108.
(101) Huang, B.; von Lilienfeld, O. A. Communication: Understanding Molecular Representations in Machine Learning: The Role of Uniqueness and Target Similarity. *J. Chem. Phys.* **2016**, *145*, No. 161102.
(102) Bannwarth, C.; Ehlert, S.; Grimme, S. GFN2-xTB—An Accurate and Broadly Parametrized Self-Consistent Tight-Binding Quantum Chemical Method with Multipole Electrostatics and Density-Dependent Dispersion Contributions. *J. Chem. Theory Comput.* **2019**, *15*, 1652−1671.
(103) Bannwarth, C.; Caldeweyher, E.; Ehlert, S.; Hansen, A.; Pracht, P.; Seibert, J.; Spicher, S.; Grimme, S. Extended Tight-Binding Quantum Chemistry Methods. *Wiley Interdiscip. Rev.: Comput. Mol. Sci.* **2021**, *11*, No. e1493.
(104) Akimov, A. V. Energy-Conserving and Thermally Corrected Neglect of Back-Reaction Approximation Method for Nonadiabatic Molecular Dynamics. *J. Phys. Chem. Lett.* **2023**, *14*, 11673−11683.
(105) Akimov, A. V. Libra: An Open-Source "Methodology Discovery" Library for Quantum and Classical Dynamics Simulations. *J. Comput. Chem.* **2016**, *37*, 1626−1649.
(106) Shakiba, M.; Smith, B.; Li, W.; Dutra, M.; Jain, A.; Sun, X.; Garashchuk, S.; Akimov, A. Libra: A Modular Software Library for Quantum Nonadiabatic Dynamics. *Software Impacts* **2022**, *14*, No. 100445.
(107) Giannini, S.; Peng, W.-T.; Cupellini, L.; Padula, D.; Carof, A.; Blumberger, J. Exciton Transport in Molecular Organic Semiconductors Boosted by Transient Quantum Delocalization. *Nat. Commun.* **2022**, *13*, No. 2755.
(108) Nelson, T.; Fernandez-Alberti, S.; Roitberg, A. E.; Tretiak, S. Electronic Delocalization, Vibrational Dynamics, and Energy Transfer in Organic Chromophores. *J. Phys. Chem. Lett.* **2017**, *8*, 3020−3031.
(109) Shakiba, M.; Stippell, E.; Li, W.; Akimov, A. V. Nonadiabatic Molecular Dynamics with Extended Density Functional Tight-Binding: Application to Nanocrystals and Periodic Solids. *J. Chem. Theory Comput.* **2022**, *18*, 5157−5180.
(110) Stanton, R.; Trivedi, D. J. Charge Carrier Dynamics at the Interface of 2D Metal−Organic Frameworks and Hybrid Perovskites for Solar Energy Harvesting. *Nano Lett.* **2023**, *23*, 11932−11939.
(111) Craig, C. F.; Duncan, W. R.; Prezhdo, O. V. Trajectory Surface Hopping in the Time-Dependent Kohn-Sham Approach for Electron-Nuclear Dynamics. *Phys. Rev. Lett.* **2005**, *95*, No. 163001.
(112) Duncan, W. R.; Craig, C. F.; Prezhdo, O. V. Time-Domain Ab Initio Study of Charge Relaxation and Recombination in Dye-Sensitized TiO_2. *J. Am. Chem. Soc.* **2007**, *129*, 8528−8543.
(113) Prezhdo, O. V.; Duncan, W. R.; Prezhdo, V. V. Photoinduced Electron Dynamics at the Chromophore−Semiconductor Interface: A Time-Domain Ab Initio Perspective. *Prog. Surf. Sci.* **2009**, *84*, 30−68.
(114) Prezhdo, O. V. Photoinduced Dynamics in Semiconductor Quantum Dots: Insights from Time-Domain Ab Initio Studies. *Acc. Chem. Res.* **2009**, *42*, 2005−2016.
(115) Prezhdo, O. V. Modeling Non-Adiabatic Dynamics in Nanoscale and Condensed Matter Systems. *Acc. Chem. Res.* **2021**, *54*, 4239−4249.
(116) Li, W.; Chen, Z.; Tang, J.; Prezhdo, O. V. Anti-Correlation between Band Gap and Carrier Lifetime in Lead Halide Perovskites under Compression Rationalized by Ab Initio Quantum Dynamics. *Chem. Mater.* **2020**, *32*, 4707−4715.

https://doi.org/10.1021/acs.jctc.4c00008
J. Chem. Theory Comput. 2024, 20, 2992−3007

(117) Chu, W.; Zheng, Q.; Prezhdo, O. V.; Zhao, J. CO2 Photoreduction on Metal Oxide Surface Is Driven by Transient Capture of Hot Electrons: Ab Initio Quantum Dynamics Simulation. *J. Am. Chem. Soc.* **2020**, *142*, 3214−3221.
(118) Kilina, S.; Ivanov, S.; Tretiak, S. Effect of Surface Ligands on Optical and Electronic Spectra of Semiconductor Nanoclusters. *J. Am. Chem. Soc.* **2009**, *131*, 7717−7726.
(119) Mai, S.; Gattuso, H.; Fumanal, M.; Muñoz-Losa, A.; Monari, A.; Daniel, C.; González, L. Excited-States of a Rhenium Carbonyl Diimine Complex: Solvation Models, Spin−Orbit Coupling, and Vibrational Sampling Effects. *Phys. Chem. Chem. Phys.* **2017**, *19*, 27240−27250.
(120) Barbatti, M. Photorelaxation Induced by Water−Chromophore Electron Transfer. *J. Am. Chem. Soc.* **2014**, *136*, 10246−10249.
(121) Smith, B.; Akimov, A. V. Hot Electron Cooling in Silicon Nanoclusters via Landau−Zener Nonadiabatic Molecular Dynamics: Size Dependence and Role of Surface Termination. *J. Phys. Chem. Lett.* **2020**, *11*, 1456−1465.
(122) Akimov, A. V. Nonadiabatic Molecular Dynamics with Tight-Binding Fragment Molecular Orbitals. *J. Chem. Theory Comput.* **2016**, *12*, 5719−5736.
(123) Akimov, A. V. Excited State Dynamics in Monolayer Black Phosphorus Revisited: Accounting for Many-Body Effects. *J. Chem. Phys.* **2021**, *155*, No. 134106.
(124) Long, R.; Fang, W.; Akimov, A. V. Nonradiative Electron−Hole Recombination Rate Is Greatly Reduced by Defects in Monolayer Black Phosphorus: Ab Initio Time Domain Study. *J. Phys. Chem. Lett.* **2016**, *7*, 653−659.
(125) Shakiba, M.; Akimov, A. V. Generalization of the Local Diabatization Approach for Propagating Electronic Degrees of Freedom in Nonadiabatic Dynamics. *Theor. Chem. Acc.* **2023**, *142*, No. 68.
(126) Hammes-Schiffer, S.; Tully, J. C. Proton Transfer in Solution: Molecular Dynamics with Quantum Transitions. *J. Chem. Phys.* **1994**, *101*, 4657−4667.
(127) Löwdin, P.-O. Quantum Theory of Many-Particle Systems. I. Physical Interpretations by Means of Density Matrices, Natural Spin-Orbitals, and Convergence Problems in the Method of Configurational Interaction. *Phys. Rev.* **1955**, *97*, 1474−1489.
(128) Nelson, T.; Fernandez-Alberti, S.; Roitberg, A. E.; Tretiak, S. Nonadiabatic Excited-State Molecular Dynamics: Treatment of Electronic Decoherence. *J. Chem. Phys.* **2013**, *138*, No. 224111.
(129) Smith, B.; Akimov, A. V. A Comparative Analysis of Surface Hopping Acceptance and Decoherence Algorithms within the Neglect of Back-Reaction Approximation. *J. Chem. Phys.* **2019**, *151*, No. 124107.
(130) Granucci, G.; Persico, M. Critical Appraisal of the Fewest Switches Algorithm for Surface Hopping. *J. Chem. Phys.* **2007**, *126*, No. 134114.
(131) Akimov, A. V.; Prezhdo, O. V. Persistent Electronic Coherence Despite Rapid Loss of Electron−Nuclear Correlation. *J. Phys. Chem. Lett.* **2013**, *4*, 3857−3864.
(132) Williams, G.; Watts, D. C. Non-Symmetrical Dielectric Relaxation Behaviour Arising from a Simple Empirical Decay Function. *Trans. Faraday Soc.* **1970**, *66*, 80−85.
(133) Wong, J. C.; Li, L.; Kanai, Y. Size Dependence and Role of Decoherence in Hot Electron Relaxation within Fluorinated Silicon Quantum Dots: A First-Principles Study. *J. Phys. Chem. C* **2018**, *122*, 29526−29536.
(134) Bussi, G.; Donadio, D.; Parrinello, M. Canonical Sampling through Velocity Rescaling. *J. Chem. Phys.* **2007**, *126*, No. 014101.
(135) Grimme, S.; Antony, J.; Ehrlich, S.; Krieg, H. A Consistent and Accurate *Ab Initio* Parametrization of Density Functional Dispersion Correction (DFT-D) for the 94 Elements H-Pu. *J. Chem. Phys.* **2010**, *132*, No. 154104.
(136) Becke, A. D. Density-Functional Exchange-Energy Approximation with Correct Asymptotic Behavior. *Phys. Rev. A* **1988**, *38*, 3098−3100.
(137) Lee, C.; Yang, W.; Parr, R. G. Development of the Colle-Salvetti Correlation-Energy Formula into a Functional of the Electron Density. *Phys. Rev. B* **1988**, *37*, 785−789.
(138) Becke, A. D. Density-functional Thermochemistry. I. The Effect of the Exchange-only Gradient Correction. *J. Chem. Phys.* **1992**, *96*, 2155−2160.
(139) Stephens, P. J.; Devlin, F. J.; Chabalowski, C. F.; Frisch, M. J. Ab Initio Calculation of Vibrational Absorption and Circular Dichroism Spectra Using Density Functional Force Fields. *J. Phys. Chem. A* **1994**, *98*, 11623−11627.
(140) Heyd, J.; Scuseria, G. E.; Ernzerhof, M. Hybrid Functionals Based on a Screened Coulomb Potential. *J. Chem. Phys.* **2003**, *118*, 8207−8215.
(141) Krukau, A. V.; Vydrov, O. A.; Izmaylov, A. F.; Scuseria, G. E. Influence of the Exchange Screening Parameter on the Performance of Screened Hybrid Functionals. *J. Chem. Phys.* **2006**, *125*, No. 224106.
(142) Goedecker, S.; Teter, M.; Hutter, J. Separable Dual-Space Gaussian Pseudopotentials. *Phys. Rev. B* **1996**, *54*, 1703−1710.
(143) Hartwigsen, C.; Goedecker, S.; Hutter, J. Relativistic Separable Dual-Space Gaussian Pseudopotentials from H to Rn. *Phys. Rev. B* **1998**, *58*, 3641−3662.
(144) Krack, M. Pseudopotentials for H to Kr Optimized for Gradient-Corrected Exchange-Correlation Functionals. *Theor. Chem. Acc.* **2005**, *114*, 145−152.
(145) Kühne, T. D.; Iannuzzi, M.; Del Ben, M.; Rybkin, V. V.; Seewald, P.; Stein, F.; Laino, T.; Khaliullin, R. Z.; Schütt, O.; Schiffmann, F.; Golze, D.; Wilhelm, J.; Chulkov, S.; Bani-Hashemian, M. H.; Weber, V.; Borštnik, U.; Taillefumier, M.; Jakobovits, A. S.; Lazzaro, A.; Pabst, H.; Müller, T.; Schade, R.; Guidon, M.; Andermatt, S.; Holmberg, N.; Schenter, G. K.; Hehn, A.; Bussy, A.; Belleflamme, F.; Tabacchi, G.; Glöß, A.; Lass, M.; Bethune, I.; Mundy, C. J.; Plessl, C.; Watkins, M.; VandeVondele, J.; Krack, M.; Hutter, J. CP2K: An Electronic Structure and Molecular Dynamics Software Package - Quickstep: Efficient and Accurate Electronic Structure Calculations. *J. Chem. Phys.* **2020**, *152*, No. 194103.
(146) Hutter, J.; Iannuzzi, M.; Schiffmann, F.; VandeVondele, J. Cp2k: Atomistic Simulations of Condensed Matter Systems. *Wiley Interdiscip. Rev.: Comput. Mol. Sci.* **2014**, *4*, 15−25.
(147) Li, W.; Long, R.; Tang, J.; Prezhdo, O. V. Influence of Defects on Excited-State Dynamics in Lead Halide Perovskites: Time-Domain Ab Initio Studies. *J. Phys. Chem. Lett.* **2019**, *10*, 3788−3804.
(148) Li, W.; Akimov, A. V. How Good Is the Vibronic Hamiltonian Repetition Approach for Long-Time Nonadiabatic Molecular Dynamics? *J. Phys. Chem. Lett.* **2022**, *13*, 9688−9694.
(149) Shakiba, M.; Akimov, A. V. *AkimovLab/Project_ML_Ham_for_NAMD: The v1.1.0 (v1.1.0)*, Zenodo, 2024.
(150) Pedregosa, F.; Varoquaux, G.; Gramfort, A.; Michel, V.; Thirion, B.; Grisel, O.; Blondel, M.; Prettenhofer, P.; Weiss, R.; Dubourg, V.; Vanderplas, J.; Passos, A.; Cournapeau, D.; et al. Scikit-Learn: Machine Learning in Python. *J. Mach. Learn. Res.* **2011**, *12*, 2825.
(151) Murphy, K. P. *Machine Learning: A Probabilistic Perspective*; MIT press, 2012.
(152) Zhang, L.; Onat, B.; Dusson, G.; McSloy, A.; Anand, G.; Maurer, R. J.; Ortner, C.; Kermode, J. R. Equivariant Analytical Mapping of First Principles Hamiltonians to Accurate and Transferable Materials Models. *npj Comput. Mater.* **2022**, *8*, No. 158.
(153) Burda, C.; Samia, A. C. S.; Hathcock, D. J.; Huang, H.; Yang, S. Experimental Evidence for the Photoisomerization of Higher Fullerenes. *J. Am. Chem. Soc.* **2002**, *124*, 12400−12401.
(154) Cimpean, C.; Groenewegen, V.; Kuntermann, V.; Sommer, A.; Kryschi, C. Ultrafast Exciton Relaxation Dynamics in Silicon Quantum Dots. *Laser Photonics Rev.* **2009**, *3*, 138−145.
(155) Reeves, K. G.; Schleife, A.; Correa, A. A.; Kanai, Y. Role of Surface Termination on Hot Electron Relaxation in Silicon Quantum Dots: A First-Principles Dynamics Simulation Study. *Nano Lett.* **2015**, *15*, 6429−6433.

https://doi.org/10.1021/acs.jctc.4c00008
J. Chem. Theory Comput. 2024, 20, 2992−3007